

GALAXY CLUSTERS SELECTED WITH THE SUNYAEV-ZEL'DOVICH EFFECT
FROM 2008 SOUTH POLE TELESCOPE OBSERVATIONS

K. VANDERLINDE,¹ T. M. CRAWFORD,^{2,3} T. DE HAAN,¹ J. P. DUDLEY,¹ L. SHAW,^{1,4} P. A. R. ADE,⁵ K. A. AIRD,⁶
 B. A. BENSON,^{7,2,8} L. E. BLEEM,^{2,9} M. BRODWIN,¹⁰ J. E. CARLSTROM,^{2,3,8,9} C. L. CHANG,^{2,8} A. T. CRITES,^{2,3} S. DESAI,¹¹
 M. A. DOBBS,¹ R. J. FOLEY,¹⁰ E. M. GEORGE,⁷ M. D. GLADDERS,^{2,3} N. R. HALL,¹² N. W. HALVERSON,¹³ F. W. HIGH,¹⁴
 G. P. HOLDER,¹ W. L. HOLZAPFEL,⁷ J. D. HRUBES,⁶ M. JOY,¹⁵ R. KEISLER,^{2,9} L. KNOX,¹² A. T. LEE,^{7,16} E. M. LEITCH,^{2,3}
 A. LOEHR,¹⁰ M. LUEKER,⁷ D. P. MARRONE,^{2,6} J. J. MCMAHON,^{2,8,17} J. MEHL,^{2,3} S. S. MEYER,^{2,8,9,3} J. J. MOHR,^{18,19,20}
 T. E. MONTROY,²¹ C.-C. NGEOW,^{11,22} S. PADIN,^{2,3} T. PLAGGE,^{7,3} C. PRYKE,^{2,3,8} C. L. REICHARDT,⁷ A. REST,¹⁴ J. RUEL,¹⁴
 J. E. RUHL,²¹ K. K. SCHAFFER,^{2,8} E. SHIROKOFF,⁷ J. SONG,¹¹ H. G. SPIELER,¹⁶ B. STALDER,¹⁰ Z. STANISZEWSKI,²¹
 A. A. STARK,¹⁰ C. W. STUBBS,^{14,10} A. VAN ENGELEN,¹ J. D. VIEIRA,^{2,9} R. WILLIAMSON,^{2,3} Y. YANG,¹¹ O. ZAHN,⁷ AND
 A. ZENTENO^{18,19}

Draft version February 14, 2022

ABSTRACT

We present a detection-significance-limited catalog of 21 Sunyaev-Zel'dovich-selected galaxy clusters. These clusters, along with 1 unconfirmed candidate, were identified in 178 deg² of sky surveyed in 2008 by the South Pole Telescope to a depth of 18 μ K-arcmin at 150 GHz. Optical imaging from the Blanco Cosmology Survey (BCS) and Magellan telescopes provided photometric (and in some cases spectroscopic) redshift estimates, with catalog redshifts ranging from $z = 0.15$ to $z > 1$, with a median $z = 0.74$. Of the 21 confirmed galaxy clusters, three were previously identified as Abell clusters, three were presented as SPT discoveries in Staniszewski et al. (2009), and three were first identified in a recent analysis of BCS data by Menanteau et al. (2010); the remaining 12 clusters are presented for the first time in this work. Simulated observations of the SPT fields predict the sample to be nearly 100% complete above a mass threshold of $M_{200} \approx 5 \times 10^{14} M_{\odot} h^{-1}$ at $z = 0.6$. This completeness threshold pushes to lower mass with increasing redshift, dropping to $\sim 4 \times 10^{14} M_{\odot} h^{-1}$ at $z = 1$. The size and redshift distribution of this catalog are in good agreement with expectations based on our current understanding of galaxy clusters and cosmology. In combination with other cosmological probes, we use this cluster catalog to improve estimates of cosmological parameters. Assuming a standard spatially flat Λ CDM cosmological model, the addition of our catalog to the WMAP 7-year results yields $\sigma_8 = 0.81 \pm 0.09$ and $w = -1.07 \pm 0.29$, a $\sim 50\%$ improvement in precision on both parameters over WMAP7 alone.

Subject headings: galaxies: clusters: individual, cosmology: observations

1. INTRODUCTION

The most massive dark matter halos to have formed so far have characteristic masses of 10^{14} to 10^{15} solar masses. Although dark matter makes up the vast majority of the mass of these objects, most observation signatures result from baryons. A small fraction of the baryons in these massive halos eventually cools to form stars and galaxies, and it was through the light from these galaxies that the most massive halos were first identified. Because of this, we generally refer to these objects as galaxy clusters, despite the small contribution of galaxies to their total mass.

Galaxy clusters are tracers of the highest peaks in the matter density field and, as such, their abundance is ex-

Electronic address: keith.vanderlinde@mail.mcgill.ca

¹ Department of Physics, McGill University, 3600 Rue University, Montreal, Quebec H3A 2T8, Canada

² Kavli Institute for Cosmological Physics, University of Chicago, 5640 South Ellis Avenue, Chicago, IL 60637

³ Department of Astronomy and Astrophysics, University of Chicago, 5640 South Ellis Avenue, Chicago, IL 60637

⁴ Department of Physics, Yale University, P.O. Box 208210, New Haven, CT 06520-8120

⁵ Department of Physics and Astronomy, Cardiff University, CF24 3YB, UK

⁶ University of Chicago, 5640 South Ellis Avenue, Chicago, IL 60637

⁷ Department of Physics, University of California, Berkeley, CA 94720

⁸ Enrico Fermi Institute, University of Chicago, 5640 South Ellis Avenue, Chicago, IL 60637

⁹ Department of Physics, University of Chicago, 5640 South Ellis Avenue, Chicago, IL 60637

¹⁰ Harvard-Smithsonian Center for Astrophysics, 60 Garden Street, Cambridge, MA 02138

¹¹ Department of Astronomy, University of Illinois, 1002 West Green Street, Urbana, IL 61801

¹² Department of Physics, University of California, One Shields Avenue, Davis, CA 95616

¹³ Department of Astrophysical and Planetary Sciences and Department of Physics, University of Colorado, Boulder, CO 80309

¹⁴ Department of Physics, Harvard University, 17 Oxford Street, Cambridge, MA 02138

¹⁵ Department of Space Science, VP62, NASA Marshall Space Flight Center, Huntsville, AL 35812

¹⁶ Physics Division, Lawrence Berkeley National Laboratory,

Berkeley, CA 94720

¹⁷ Department of Physics, University of Michigan, 450 Church Street, Ann Arbor, MI, 48109

¹⁸ Department of Physics, Ludwig-Maximilians-Universität, Scheinerstr. 1, 81679 München, Germany

¹⁹ Excellence Cluster Universe, Boltzmannstr. 2, 85748 Garching, Germany

²⁰ Max-Planck-Institut für extraterrestrische Physik, Giessenbachstr. 85748 Garching, Germany

²¹ Physics Department and CERCA, Case Western Reserve University, 10900 Euclid Ave., Cleveland, OH 44106

²² Graduate Institute of Astronomy, National Central University, No. 300 Jonghda Rd, Jhongli City, 32001, Taiwan

ponentially sensitive to the growth of structure over cosmic time. A measurement of the abundance of galaxy clusters as a function of mass and redshift has the power to constrain cosmological parameters to unprecedented levels (Wang & Steinhardt 1998; Haiman et al. 2001; Holder et al. 2001; Battye & Weller 2003; Molnar et al. 2004; Wang et al. 2004; Lima & Hu 2007), assuming that the selection criteria are well understood. To usefully constrain the growth history of large scale structure, a sample of galaxy clusters must cover a wide redshift range. Furthermore, the observable property with which the clusters are selected should correlate strongly with halo mass, which is the fundamental quantity predicted from theory and simulations. The thermal Sunyaev Zel'dovich (SZ; Sunyaev & Zel'dovich 1972) signatures of galaxy clusters provide nearly these selection criteria. Surveys of galaxy clusters based on the SZ effect have consequently been eagerly anticipated for over a decade. This paper presents the first cosmologically meaningful catalog of galaxy clusters selected via the thermal SZ effect.

1.1. The Thermal SZ Effect

The vast majority of known galaxy clusters have been identified by their optical properties or from their X-ray emission. Clusters of galaxies contain anywhere from several tens to many hundreds of galaxies, but these galaxies account for a small fraction of the total baryonic mass in a cluster. Most of the baryons in clusters are contained in the intra-cluster medium (ICM), the hot ($\sim 10^7 - 10^8$ K) X-ray-emitting plasma that pervades cluster environments. Sunyaev & Zel'dovich (1972) noted that this same plasma should also interact with cosmic microwave background (CMB) photons via inverse Compton scattering, causing a small spectral distortion of the CMB along the line of sight to a cluster.

The thermal SZ effect has been observed in dozens of known clusters (clusters previously identified in the optical or X-ray) over the last few decades (Birkinshaw 1999; Carlstrom et al. 2002). However, it was not until very recently that the first previously unknown clusters were identified through their thermal SZ effect (Staniszewski et al. 2009). This is mostly due to the small amplitude of the effect. The magnitude of the temperature distortion at a given position on the sky is proportional to the integrated electron pressure along the line of sight. At the position of a massive galaxy cluster, this fluctuation is only on the order of a part in 10^4 , or a few hundred μK^1 . It is only with the current generation of large (\sim kilopixel) detector arrays on 6-12 m telescopes (Fowler et al. 2007; Carlstrom et al. 2009) that large areas of sky are being surveyed to depths sufficient to detect signals of this amplitude.

A key feature of the SZ effect is that the SZ surface brightness is insensitive to the redshift of the cluster. As a spectral distortion of the CMB (rather than an intrinsic emission feature), SZ signals redshift along with the CMB. A given parcel of gas will imprint the same spec-

tral distortion on the CMB regardless of its cosmological redshift, depending only on the electron density n_e and temperature T_e . This makes SZ surveys an excellent technique for discovering clusters over a wide redshift range.

Another aspect of the thermal SZ effect that makes it especially attractive for cluster surveys is that the integrated thermal SZ flux is a direct measure of the total thermal energy of the ICM. The SZ flux is thus expected to be a robust proxy for total cluster mass (Barbosa et al. 1996; Holder & Carlstrom 2001; Motl et al. 2005).

A mass-limited cluster survey across a wide redshift range provides a growth-based test of dark energy to complement the distance based tests provided by supernovae (Perlmutter et al. 1999; Schmidt et al. 1998). Recent results (e.g., Vikhlinin et al. 2009; Mantz et al. 2010), have demonstrated the power of such tests to constrain cosmological models and parameters.

1.2. The SPT SZ Cluster Survey

The South Pole Telescope (SPT) (Carlstrom et al. 2009) is a 10-meter off-axis telescope optimized for arcminute-resolution studies of the microwave sky. It is currently conducting a survey of a large fraction of the southern sky with the principal aim of detecting galaxy clusters via the SZ effect. In 2008, the SPT surveyed $\sim 200 \text{ deg}^2$ of the microwave sky with an array of 960 bolometers operating at 95, 150, and 220 GHz. Using 40 deg^2 of these data (and a small amount of overlapping data from 2007), Staniszewski et al. (2009) (hereafter S09) presented the first discovery of previously unknown clusters by their SZ signature. Lueker et al. (2010) (hereafter L10) used $\sim 100 \text{ deg}^2$ of the 2008 survey to measure the power spectrum of small scale temperature anisotropies in the CMB, including the first significant detection of the contribution from the SZ secondary anisotropy.

In this paper we expand upon the results in S09 and present an SZ-detection-significance-limited catalog of galaxy clusters identified in the 2008 SPT survey. Redshifts for 21 of these objects have been obtained from follow-up optical imaging, the details of which are discussed in a companion paper (High et al. 2010). Using simulated observations we characterize the SPT cluster selection function — the detectability of galaxy clusters in the survey as a function of mass and redshift — for the 2008 fields. A simulation-based mass scaling relation allows us to compare the catalog to theoretical predictions and place constraints on the normalization of the matter power spectrum on small scales, σ_8 , and the dark energy equation of state parameter w .

This paper is organized as follows: §2 discusses the observations, including data reduction, mapmaking, filtering, cluster-finding, optical follow-up and cluster redshift estimation; §3 presents the resulting cluster catalog; §4 provides a description of our estimate of the selection function; §5 investigates the sample in the context of our current cosmological understanding and derives parameter constraints; we discuss limitations and possible contaminants in §6, and we close with a discussion in §7.

For our fiducial cosmology we assume a spatially flat Λ CDM model (parameterized by $\Omega_b h^2$, $\Omega_c h^2$, H_0 , n_s , τ , and A_{002}) with parameters consistent with the WMAP

¹ Throughout this work, the unit K refers to equivalent fluctuations in the CMB temperature, i.e., the level of temperature fluctuation of a 2.73 K blackbody that would be required to produce the same power fluctuation. The conversion factor is given by the derivative of the blackbody spectrum, $\frac{dB}{dT}$, evaluated at 2.73 K.

5-year Λ CDM best-fit results (Dunkley et al. 2009)², namely $\Omega_M = 0.264$, $\Omega_b = 0.044$, $h = 0.71$, $\sigma_8 = 0.80$. All references to cluster mass refer to M_{200} , the mass enclosed within a spherical region of mean overdensity $200 \times \rho_{mean}$, where ρ_{mean} is the mean matter density on large scales at the redshift of the cluster.

2. OBSERVATIONS, DATA REDUCTION, CLUSTER EXTRACTION, AND OPTICAL FOLLOW-UP

2.1. Observations

The results presented in this work are based on observations performed by the SPT in 2008. Carlstrom et al. (2009) and S09 describe the details of these observations; we briefly summarize them here. Two fields were mapped to the nominal survey depth in 2008: one centered at right ascension (R.A.) $5^h 30^m$, declination (decl.) -55° (J2000), hereafter the 5^h field; and one centered at R.A. $23^h 30^m$, decl. -55° , hereafter the 23^h field. Results in this paper are based on roughly 1500 hours of observing time split between the two fields. The areas mapped with near uniform coverage were 91 deg^2 in the 5^h field and 105 deg^2 in the 23^h field.

This work considers only the 150 GHz data from the uniformly covered portions of the 2008 fields. The detector noise for the 95 GHz detectors was very high for the 2008 season, and the 220 GHz observations were contaminated by the atmosphere at large scales where they would be useful for removing CMB fluctuations. Including these bands did not significantly improve the efficiency of cluster detections and they were not used in the analysis presented here. The final depth of the 150 GHz maps of the two fields is very similar, with the white noise level in each map equal to $18 \mu\text{K-arcmin}$.

The two fields were observed using slightly different scan strategies. For the 5^h field, the telescope was swept in azimuth at a constant velocity ($\sim 0.25^\circ/\text{s}$ on the sky at the field center) across the entire field then stepped in elevation, with this pattern continuing until the whole field was covered. The 23^h field was observed using a similar strategy, except that the azimuth scans covered only one half of the field at any one time, switching halves each time one was completed. One consequence of this observing strategy was that a narrow strip in the middle of the 23^h field received twice as much detector time as the rest of the map. The effect of this strip on our catalog is minimal and is discussed in §4.6.

A single observation of either field lasted ~ 2 hours. Between individual observations, several short calibration measurements were performed, including measurements of a chopped thermal source, 2 degree elevation nods, and scans across the galactic HII regions RCW38 and MAT5a. This series of regular calibration measurements was used to identify detectors with good performance, assess relative detector gains, monitor atmospheric opacity and beam parameters, and model pointing variations.

2.2. Data processing and mapmaking

The data reduction pipeline applied to SPT data in this work is very similar to that used in S09. Broadly,

² These parameters are sufficiently similar to the WMAP 7-year preferred cosmology (Larson et al. 2010) that a re-analysis based on that newer work is not warranted.

the pipeline for both fields consists of filtering the time-ordered data from each individual detector, reconstructing the pointing for each detector, and combining data from all detectors in a given observing band into a map by simple inverse-variance-weighted binning and averaging.

The small differences between the data reduction used in this work and that of S09 are:

- In S09, a 19th-order polynomial was fit and removed from each detector's timestream on each scan across the field. Samples in the timestream which mapped to positions on the sky near bright point sources were excluded from the fit. A similar subtraction was performed here, except that a first-order polynomial was removed, supplemented by sines and cosines (Fourier modes). Frequencies for the Fourier modes were evenly spaced from 0.025 Hz to 0.25 Hz. This acts approximately as a high-pass filter in the R.A. direction with a characteristic scale of $\sim 1^\circ$ on the sky.
- In S09, a mean across functioning detectors was calculated at each snapshot in time and subtracted from each sample. Here, both a mean and a slope across the two-dimensional array were calculated at each time and subtracted. This acts as a roughly isotropic spatial high-pass filter, with a characteristic scale of $\sim 0.5^\circ$.
- As in Vieira et al. (2010), a small pointing correction ($\sim 5''$ on the sky) was applied, based on comparisons of radio source positions derived from SPT maps and positions of those sources in the AT20G catalog (Murphy et al. 2010).

The relative and absolute calibrations of detector response were performed as in L10. The relative gains of the detectors and their gain variations over time were estimated using measurements of their response to a chopped thermal source. These relative calibrations were then tied to an absolute scale through direct comparison of WMAP 5-year maps (Hinshaw et al. 2009) to dedicated large-area SPT scans. This calibration is discussed in detail in L10, and is accurate to 3.6% in the 150 GHz data.

2.3. Cluster Extraction

The cluster extraction procedure used in this work for both fields is identical to the procedure used in S09, where more details can be found.

The SPT maps were filtered to optimize detection of objects with morphologies similar to the SZ signatures expected from galaxy clusters, through the application of spatial matched filters (Haehnelt & Tegmark 1996; Herranz et al. 2002a,b; Melin et al. 2006). In the spatial Fourier domain, the map was multiplied by

$$\psi(k_x, k_y) = \frac{B(k_x, k_y)S(|\vec{k}|)}{B(k_x, k_y)^2 N_{astro}(|\vec{k}|) + N_{noise}(k_x, k_y)}$$

where ψ is the matched filter, B is the response of the SPT instrument after timestream processing to signals on the sky, S is the assumed source template, and the noise power has been broken into astrophysical (N_{astro})

and noise (N_{noise}) components. For the source template, a projected spherical β -model, with β fixed to 1, was used:

$$\Delta T = \Delta T_0 (1 + \theta^2 / \theta_c^2)^{-1},$$

where the normalization ΔT_0 and the core radius θ_c are free parameters.

The noise power spectrum N_{noise} includes contributions from atmospheric and instrumental noise, while N_{astro} includes power from primary and lensed CMB fluctuations, an SZ background, and point sources. The atmospheric and instrumental noise were estimated from jackknife maps as in S09, the CMB power spectrum was updated to the lensed CMB spectrum from the WMAP5 best-fit Λ CDM cosmology (Dunkley et al. 2009), the SZ background level was assumed to be flat in $\ell(\ell + 1)C_\ell$ with the amplitude taken from L10, and the point source power was assumed to be flat in C_ℓ at the level given in Hall et al. (2010).

To avoid spurious decrements from the wings of bright point sources, all positive sources above a given flux (roughly 7 mJy, or 5σ in a version of the map filtered to optimize point-source signal-to-noise) were masked to a radius of $4'$ before the matched filter was applied. Roughly 150 sources were masked in each field, of which 90–95% are radio sources. The final sky areas considered after source masking were 82.4 and 95.1 deg² for the 5^h and 23^h fields respectively.

The maps were filtered for twelve different cluster scales, constructed using source templates with core radii θ_c evenly spaced between 0.25' to 3.0'. Each filtered map M_{ij} , where i refers to the filter scale and j to the field, was then divided into strips corresponding to distinct $90'$ ranges in elevation. The noise was estimated independently in each strip in order to account for the weak elevation dependence of the survey depth. The noise in the k^{th} strip of map M_{ij} , σ_{ijk} , was estimated as the standard deviation of the map within that strip.

Signal-to-noise maps \tilde{M}_{ij} were then constructed by dividing each strip k in map M_{ij} by σ_{ijk} . SZ cluster decrements were identified in each map \tilde{M}_{ij} by a simple (negative) peak detection algorithm similar to SExtractor (Bertin & Arnouts 1996). The highest signal-to-noise value associated with a decrement, across all filter scales, was defined as ξ , and taken as the significance of a detection. Candidate clusters were identified in the data down to ξ of 3.5, though this work considers only the subset with $\xi \geq 5$.

These detection significances are robust against choice of source template: the use of Nagai (Nagai et al. 2007), Arnaud (Arnaud et al. 2010) or Gaussian templates in place of β -models was found to be free of bias and to introduce negligible ($\sim 2\%$) scatter on recovered ξ .

2.4. Optical Imaging and Spectroscopy

Optical imaging was used for confirmation of candidates, for photometric redshift estimation, and for cluster richness characterization. A detailed description of the coordinated optical effort is presented in High et al. (2010) and is summarized here.

The 5^h and 23^h fields were selected in part for overlap with the Blanco Cosmology Survey (BCS, see Ngeow et al. 2009), which consists of deep optical images using g , r , i and z filters. These images, obtained from

the Blanco 4m telescope at CTIO with the MOSAIC-II imager in 2005–2007, were used when available. The co-added BCS images have 5σ galaxy detection thresholds of 24.75, 24.65, 24.35 and 23.05 magnitude in *griz*, respectively.

For clusters that fell outside the BCS coverage region, as well as for 5 that fell within, and for the unconfirmed candidate, images were obtained using the twin 6.5 m Magellan telescopes at Las Campanas, Chile. The imaging data on Magellan were obtained by taking successively deeper images until a detection of the early-type cluster galaxies was achieved, complete to between L^* and $0.4L^*$ in at least one band. The Magellan images were obtained under a variety of conditions, and the Stellar Locus Regression technique (High et al. 2009) was used to obtain precise colors and magnitudes.

Spectroscopic data were obtained for a subset of the sample using the Low Dispersion Survey Spectrograph on Magellan (LDSS3, see Osip et al. 2008) in longslit mode. Typical exposures were 20–60 minutes, with slit orientations that contained the brightest cluster galaxy (BCG) and as many additional red cluster members as possible.

Photometric redshifts were estimated using standard red sequence techniques and verified using the spectroscopic subsample. A red sequence model was derived from the work of Bruzual & Charlot (2003), and local overdensities of red galaxies were searched for near the cluster candidate positions. By comparing the resulting photo- z 's to spectroscopic redshifts within the subsample of 10 clusters for which spectroscopic data are available, H10 estimates photo- z uncertainty σ_z as given in Table 1, of order 3% in $(1 + z)$.

Completeness in red sequence cluster finding was estimated from mock catalogs. At BCS depths, galaxy cluster completeness for the masses relevant for this sample is nearly unity up to a redshift of one, above which the completeness falls rapidly, reaching 50% at about redshift 1.2, and 0% at redshift 1.25. At depths about a magnitude brighter (corresponding to the depth of the Magellan observations of the unconfirmed candidate, §3.1), the completeness deviates from unity at redshift ~ 0.8 .

3. CATALOG

The resulting catalog of galaxy clusters, complete for $\xi \geq 5$, is presented in Table 1. Simulations (§4.1) suggest that this catalog should be highly complete above limiting mass and redshift thresholds, with relatively low contamination.

A total of 22 candidates were identified, for which optical follow-up confirmed and obtained redshift information on all but one. Three clusters were previously known from X-ray and optical surveys, three were previously reported from this survey by S09, three were first identified in a recent analysis of BCS data by Menanteau et al. (2010), and the remainder are new discoveries. Detailed comparisons of the SPT and Menanteau et al. (2010) cluster catalogs and selection will be the subject of future work.

Thumbnail images of the signal-to-noise maps, \tilde{M} , at the preferred filter scale for each cluster are provided in Appendix A, Figure A1. Signal-to-noise as a function of filter scale for each cluster is shown in Appendix A, Figure A2.

TABLE 1
THE SPT CLUSTER CATALOG FOR THE 2008 OBSERVING SEASON

Object Name	R.A.	decl.	ξ	θ_c	Photo-z	σ_z	Spec-z	Opt
SPT-CL J0509-5342 ^{†‡}	77.336	-53.705	6.61	0.50	0.47	0.04	0.4626	BCS+Mag
SPT-CL J0511-5154 ^a	77.920	-51.904	5.63	0.50	0.74	0.05	-	Mag
SPT-CL J0516-5430 ^{†‡b}	79.148	-54.506	9.42	0.75	0.25	0.03	0.2952	BCS+Mag
SPT-CL J0521-5104 ^{‡c}	80.298	-51.081	5.45	1.00	0.72	0.05	-	BCS
SPT-CL J0528-5300 ^{†d}	82.017	-53.000	5.45	0.25	0.75	0.05	0.7648	BCS+Mag
SPT-CL J0533-5005	83.398	-50.092	5.59	0.25	0.83	0.05	0.8810	Mag
SPT-CL J0539-5744 [‡]	85.000	-57.743	5.12	0.25	0.77	0.05	-	Mag
SPT-CL J0546-5345 ^{†‡}	86.654	-53.761	7.69	0.50	1.16	0.06	-	BCS
SPT-CL J0551-5709 ^{‡e}	87.902	-57.156	6.13	1.00	0.41	0.04	0.4230	Mag
SPT-CL J0559-5249 [‡]	89.925	-52.826	9.28	1.00	0.66	0.04	0.6112	Mag
SPT-CL J2259-5617 ^{†f}	344.997	-56.288	5.29	0.25	0.16	0.03	0.1528	Mag
SPT-CL J2300-5331 ^{†g}	345.176	-53.517	5.29	0.25	0.29	0.03	-	Mag
SPT-CL J2301-5546	345.469	-55.776	5.19	0.50	0.78	0.05	-	Mag
SPT-CL J2331-5051	352.958	-50.864	8.04	0.25	0.55	0.04	0.5707	Mag
SPT-CL J2332-5358 ^{†h}	353.104	-53.973	7.30	1.50	0.32	0.03	-	BCS+Mag
SPT-CL J2337-5942 [‡]	354.354	-59.705	14.94	0.25	0.77	0.05	0.7814	Mag
SPT-CL J2341-5119	355.299	-51.333	9.65	0.75	1.03	0.05	0.9983	Mag
SPT-CL J2342-5411	355.690	-54.189	6.18	0.50	1.08	0.06	-	BCS
SPT-CL J2343-5521	355.757	-55.364	5.74	2.50	-	-	-	BCS+Mag
SPT-CL J2355-5056	358.955	-50.937	5.89	0.75	0.35	0.04	-	Mag
SPT-CL J2359-5009	359.921	-50.160	6.35	1.25	0.76	0.05	-	Mag
SPT-CL J0000-5748	0.250	-57.807	5.48	0.50	0.74	0.05	-	Mag

NOTE. — Recall that ξ is the maximum signal-to-noise obtained over the set of filter scales for each cluster. The θ_c (given in arcminutes) refer to the preferred filter scale, that at which ξ was found. Cluster positions in R.A. and decl. are given in degrees, and refer to the center of SZ brightness in map filtered at the preferred scale, calculated as the mean position of all pixels associated with the detection, weighted by their SZ brightness. The four rightmost columns refer to optical follow-up observations, giving the measured photometric redshift measurements and uncertainties of the optical counterpart, spectroscopic redshifts where available, and the source (BCS or Magellan) of the follow-up data.

[†]Clusters identified in S09. The cluster names have been updated (clusters were identified as SPT-CL 0509-5342, SPT-CL 0517-5430, SPT-CL 0528-5300, and SPT-CL 0547-5345 in S09) in response to an IAU naming convention request, an improved pointing model, and the updated data processing.

[‡]Clusters within 2' of RASS sources (RASS-FSC, RASS-BSC; Voges et al. 2000, 1999).

^aSCSO J051145-515430 (Menanteau et al. 2010).

^bAbell S0520 (Abell et al. 1989), RXCJ0516.6-5430 (Böhringer et al. 2004), SCSO J051637-543001 (Menanteau et al. 2010).

^cSCSO J052113-510418 (Menanteau et al. 2010).

^dSCSO J052803-525945 (Menanteau et al. 2010).

^eAbell S0552 (Abell et al. 1989) is in the foreground, 5' away at $z=0.09$ (this redshift not previously measured).

^fAbell 3950 (Abell et al. 1989). Spectroscopic redshift from Jones et al. (2005).

^gAbell S1079 (Abell et al. 1989, redshift shown not previously measured).

^hSCSO J233227-535827 (Menanteau et al. 2010).

Estimates of cluster masses are possible with the aid of a scaling relation (below, §4.8), and are discussed in Appendix D.

3.1. Noteworthy Clusters

SPT-CL 2259-5617— The SZ signal from this cluster is anomalously compact for such a low redshift object. The cosmological analysis (§5) explicitly excludes all $z < 0.3$ clusters, so this cluster not used in parameter estimation.

SPT-CL J2331-5051— This cluster appears to be one of a pair of clusters at comparable redshift, likely undergoing a merger. It will be discussed in detail in a future publication. The fainter partner is not included in this catalog as its significance ($\xi = 4.81$) falls below the detection threshold.

SPT-CL J2332-5358— This cluster is coincident with a bright dusty point source which we identify in the 23h 220 GHz data. Although the 150 GHz flux from this

source could be removed with the aid of the 220 GHz map, a multi-frequency analysis is outside the scope of the present work. The impact of point sources on the resulting cluster catalog is discussed in §6.2.

SPT-CL J2343-5521— No optical counterpart was found for this candidate. The field was imaged with both BCS and Magellan, and no cluster of galaxies was found to a 5σ point source detection depth. The simulated optical completeness suggests that this candidate is either a false positive in the SPT catalog or a cluster at high redshift ($z \gtrsim 1.2$). While the relatively high $\xi = 5.74$ indicates a $\sim 7\%$ chance of a false detection in the SPT survey area (see discussion of contamination below, §4.7), the signal-to-noise of this detection exhibits peculiar behavior with θ_c (see Figure A2), preferring significantly larger scales than any other candidate, consistent with a CMB decrement. Further multi-wavelength follow-up observations are underway on this candidate, and preliminary results indicate it is likely a false detection.

3.2. Recovering integrated SZ flux

The optimal filter described in §2.3 provides an estimate of the β -model normalization, ΔT_0 , and core size for each cluster, based on the filter scale θ_c at which the significance ξ was maximized. Assuming prior knowledge of the ratio θ_{200}/θ_c (where θ_{200} is the angle subtending the physical radius R_{200} at the redshift of the cluster), one can integrate the β -profile to obtain an estimate of the integrated SZ flux, Y . Basic physical arguments and hydrodynamical simulations of clusters have demonstrated Y to be a tight (low intrinsic scatter) proxy for cluster mass (Barbosa et al. 1996; Holder & Carlstrom 2001; Motl et al. 2005; Nagai et al. 2007; Stanek et al. 2010).

In single-frequency SZ surveys, the primary CMB temperature anisotropies provide a source of astrophysical contamination that greatly inhibits an accurate measure of θ_c (Melin et al. 2006). The modes at which the primary CMB dominates must be filtered out from the map, significantly reducing the range of angular scales that can be used by the optimal filter to constrain θ_c . This range is already limited by the $\sim 1'$ instrument beam, which only resolves θ_c for the larger clusters. Any integrated quantity will thus be poorly measured. Melin et al. (2006) demonstrated that if the value of θ_c can be provided by external observations, e.g., X-ray, Y can be accurately measured.

The inability to constrain θ_c can be seen in Figure A2, where the highest signal-to-noise associated with a peak is plotted against each filter scale. For several clusters (for example, SPT-CL J0516-5430, SPT-CL J0551-5709, and SPT-CL J2332-5358), the peak in signal-to-noise associated with a cluster is very broad in θ_c . Because of this confusion, we do not report Y in this work. Instead, as described below (§4.8), we use detection significance as a proxy for mass.

Multi-frequency surveys are not in principle subject to this limitation as the different frequencies can be combined to eliminate sources of noise that are correlated between bands, thus increasing the range of angular scales available for constraining cluster profiles.

4. SZ SELECTION FUNCTION

In this section, we characterize the SPT cluster sample identified in Table 1. Specifically, we describe the SPT cluster selection function in terms of the catalog completeness as a function of mass and redshift, and the contamination rate. This selection function was determined by applying the cluster detection algorithm described in §2.3 to a large number of simulated SPT observations. These simulations included the dominant astrophysical components (primary and lensed CMB, cluster thermal SZ, and two families of point sources), accounted for the effects of the SPT instrument and data processing (the “transfer function”), and contained realistic atmospheric and detector noise.

4.1. Simulated thermal SZ Cluster Maps

Simulated SZ maps were generated using the method of Shaw et al. (2009), where a detailed description of the procedure can be found. In brief, the semi-analytic gas model of Bode et al. (2007) was applied to halos identified in the output of a large dark matter lightcone simulation.

The cosmological parameters for this simulation were chosen to be consistent with those measured from the WMAP 5-year data combined with large-scale structure observations (Dunkley et al. 2009), namely $\Omega_M = 0.264$, $\Omega_b = 0.044$, and $\sigma_8 = 0.8$. The simulated volume was a periodic box of size 1 Gpc/h. The matter distribution in 421 time slices was arranged into a lightcone covering a single octant of the sky from $0 < z \leq 3$.

Dark matter halos were identified and gas distributions were calculated for each halo using the semi-analytic model of Bode et al. (2007). This model assumes that intra-cluster gas resides in hydrostatic equilibrium in the gravitational potential of the host dark matter halo with a polytropic equation of state. As discussed in Bode et al. (2007), the most important free parameter is the energy input into the cluster gas via non-thermal feedback processes, such as supernovae and outflows from active galactic nuclei (AGN). This is set through the parameter ϵ_f such that the feedback energy is $E_f = \epsilon_f M_* c^2$, where M_* is the total stellar mass in the cluster. Bode et al. (2007) calibrate ϵ_f by comparing the model against observed X-ray scaling relations for low redshift ($z < 0.25$) group and cluster mass objects. We note that the redshift range in which the model has been calibrated and that encompassed by the cluster sample presented here barely overlap; comparison of the model to the SPT sample (as, for example, in §5) thus provides a test of the predicted cluster and SZ signal evolution at high redshift.

For our fiducial model we adopt $\epsilon_f = 5 \times 10^{-5}$, however for comparison we also generate maps using the ‘standard’ and ‘star-formation only’ versions of this model described in Bode et al. (2009). There are two principal differences between these models. First, the stellar mass fraction M_*/M_{gas} is constant with total cluster mass in the fiducial model, but mass-dependent in the ‘standard’ and ‘star-formation’ model. Second, the amount of energy feedback is significantly lower in the ‘standard’ than model than in the fiducial, and zero in the ‘star-formation’ model.

From the output of each model, a 2-d image of SZ intensity for each cluster with mass $M > 5 \times 10^{13} M_\odot h^{-1}$ was produced by summing up the electron pressure along the line of sight. SZ cluster sky maps were constructed by projecting down the lightcone, summing up the contribution of all the clusters along the line of sight. Individual SZ sky maps were 10×10 degrees in size, resulting in a total of 40 independent maps. For each map, the mass, redshift, and position of each cluster was recorded.

From SPT pointed observations of X-ray-selected clusters, Plagge et al. (2010) have demonstrated that cluster radial SZ profiles match the form of the “universal” electron pressure profile measured by Arnaud et al. (2010) from X-ray observations of massive, low-redshift clusters. To complement the set of maps generated using the semi-analytic gas model, SZ sky maps were generated in which the projected form of the Arnaud et al. (2010) pressure profile was used to generate the individual cluster SZ signals.

4.2. Point Source Model

At 150 GHz and at the flux levels of interest to this analysis (~ 1 to ~ 10 mJy), the extragalactic source population is expected to be primarily composed of two broad classes: sources dominated by thermal emission

from dust heated by a burst of star formation, and sources dominated by synchrotron emission from AGN. We refer to these two families as “dusty sources” and “radio sources” and include models for both in our simulated observations.

For dusty sources, the source count model of Negrello et al. (2007) at 350 GHz was used. These counts are based on the physical model of Granato et al. (2004) for high-redshift SCUBA-like sources and on a more phenomenological approach for late-type galaxies (starburst plus normal spirals). Source counts were estimated at 150 GHz by assuming a scaling for the flux densities of $S_\nu \propto \nu^\alpha$, with $\alpha = 3$ for high-redshift protospheroidal galaxies and $\alpha = 2$ for late-type galaxies. For radio sources, the de Zotti et al. (2005) model for counts at 150 GHz was used. This model is consistent with the measurements of Vieira et al. (2010) for the radio source population at 150 GHz.

Realizations of source populations were generated by sampling from Poisson distributions for each population in bins with fluxes from 0.01 mJy to 1000 mJy. Sources were distributed in a random way across the map. Correlations between sources or with galaxy clusters were not modeled, and we discuss this potential contamination in §6.2.

4.3. CMB Realizations

Simulated CMB anisotropies were produced by generating sky realizations based on the power in the gravitationally lensed WMAP 5-year Λ CDM CMB power spectrum. Non-gaussianity in the lensed power was not modeled.

4.4. Transfer Function

The effects of the transfer function, i.e., the effects of the instrument beam and the data processing on sky signal, were emulated by producing synthetic SPT timestreams from simulated skies sampled using the same scans employed in the observations. The sky signal was convolved with the measured SPT 150 GHz beam, timestream samples were convolved with detector time constants, and the SPT data processing (§2.2) was performed on the simulated timestreams to produce maps.

Full emulation of the transfer function is a computationally intensive process; to make a large number of simulated observations, the transfer function was modeled as a 2D Fourier filter. The accuracy of this approximation was measured by comparing recovered ξ of simulated clusters in skies passed through the full transfer function against the ξ of the same clusters when the transfer function was approximated as a Fourier filter applied to the map. Systematic differences were found to be less than 1% and on an object-by-object basis the two methods produced measured ξ that agreed to better than 3%.

4.5. Instrumental & Atmospheric Noise

Noise maps were created from SPT data by subtracting one half of each observation from the other half. Within each observation, one direction (azimuth either increasing or decreasing) was chosen at random, and all data when the telescope was moving in that direction were multiplied by -1. The data were then processed and combined as usual to produce a “jackknife” map which con-

tained the full noise properties of the final field map, but with all sky signal removed.

4.6. The 23^h Deep Strip

Due to the observing strategy employed on the 23^h field, a $\sim 1.5^\circ$ strip in the middle of that map contains significantly lower atmospheric and instrumental noise than the rest of the map. The jackknife noise maps (§4.5) used in simulated observations naturally include this deep strip, so any effects due to this feature are taken into account in the simulation-based estimation of the average selection function (§4.7) and scaling relation (§4.8) across the whole survey region. The cosmological analysis (§5) uses these averaged quantities; simulated observations performed with and without a deep strip demonstrated that any bias or additional scatter from using the averaged quantities is negligible compared to the statistical errors.

4.7. Completeness and Contamination

Forty realizations of the 2008 SPT survey (two fields each) were simulated, from which clusters were extracted and matched against input catalogs.

Figure 1 shows the completeness of the simulated SPT sample, the fraction of clusters in simulated SPT maps that were detected with $\xi \geq 5$, as a function of mass and redshift. The exact shape and location of the curves in this figure depend on the detailed modeling of intra-cluster physics, which remain uncertain. The increase in SZ brightness (and cluster detectability) with increasing redshift at fixed mass is due to the increased density and temperature of high redshift clusters, and is in keeping with self-similar evolution. At low redshifts ($z \lesssim 0.3$), CMB confusion suppresses cluster detection significances and drives a strong low-redshift evolution in the selection function. These completeness curves were not used in the cosmological analysis (§5), where uncertainties on the mass scaling relation (§4.8) account for uncertainties in the modeling of intra-cluster physics.

The SZ sky was removed from simulations to estimate the rate of false positives in the SPT sample. Figure 2 shows this contamination rate as a function of lower ξ threshold, averaged across the survey area. A $\xi \geq 5$ threshold leads to approximately one false detection within the survey area.

To test for biases introduced by an SZ background composed of low-mass systems, a simulation was run including only SZ sources well below the SPT threshold, with masses $M < 10^{14} M_\odot h^{-1}$. This background was found to have negligible effect on the detection rate as compared to the SZ-free false detection simulation.

4.8. Mass Scaling Relation

As discussed in §3.2, the integrated SZ flux Y is poorly estimated in this analysis and so is not used as a mass proxy. However, the noise σ_{ijk} measured in each elevation strip is relatively even across the SPT maps, so it is possible to work in the native space of the SPT selection function and use detection significance ξ as proxy for mass. Additional uncertainty and bias introduced by use of such a relation (in place of, for example, a Y -based scaling relation) are small compared to the Poisson noise of the sample and the uncertainties in modeling intra-cluster physics.

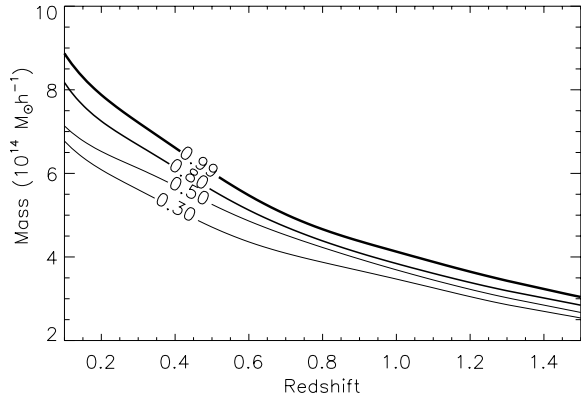


FIG. 1.— Simulated catalog completeness as a function of mass and redshift for a significance cut of $\xi \geq 5$. The contours show lines of constant completeness. From left to right, the lines represent 30, 50, 80 and 99% completeness. The temperature and density of clusters at a given mass tends to increase with redshift, leading to the increased SZ flux and improved detectability of high-redshift clusters. The strong evolution below $z \sim 0.3$ arises from reduced ξ on nearby clusters due to CMB confusion. Note that these contours are based on the fiducial simulations used in this work. Uncertainties in modeling (discussed in §4.8) can shift the position and shape of these contours coherently but significantly (of order 30% in mass).

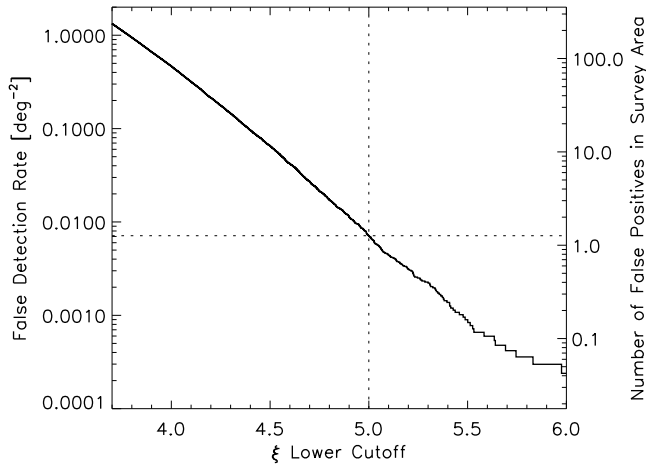


FIG. 2.— Simulated false detection rate, averaged across the survey area. The left axis shows the number density of false detections above a given ξ ; the right axis shows the equivalent number of false detections within the combined 5^h and 23^h survey fields. The dotted lines show the $\xi \geq 5$ threshold applied to the catalog, and the false detection rate at that threshold, ~ 1.2 across the full survey area.

The steepness of the cluster mass function in the presence of noise will result in a number of detections that have boosted significance. Explicitly, ξ is a biased estimator for $\langle \xi \rangle$, the average detection significance of a given cluster across many noise realizations. An additional bias on ξ comes from the choice to maximize signal-to-noise across three free parameters, R.A., decl. and θ_c . These biases make the relation between ξ and mass complex and difficult to characterize.

In order to produce a mass scaling relation with a simple form, the unbiased significance ζ is introduced. It is defined as the average detection signal-to-noise of a simulated cluster, measured across many noise realizations,

evaluated at the preferred position and filter scale of that cluster as determined by fitting the cluster in the absence of noise.

Relating ζ and ξ is a two step process. The expected relation between ζ and $\langle \xi \rangle$ is derived and compared to simulated observations in Appendix B, and found to be $\zeta = \sqrt{\langle \xi \rangle^2 - 3}$. Given a known $\langle \xi \rangle$, the expected distribution in ξ is derived by convolution with a Gaussian of unit width. The relation between ζ and $\langle \xi \rangle$ is taken to be exact, and was verified through simulations to introduce negligible additional scatter; i.e., the scatter in the ζ - ξ relation is the same as the scatter in the $\langle \xi \rangle$ - ξ relation, namely a Gaussian of unit width.

The scaling between ζ and M is assumed to take the form of power-law relations with both mass and redshift:

$$\zeta = A \left(\frac{M}{5 \times 10^{14} M_\odot h^{-1}} \right)^B \left(\frac{1+z}{1.6} \right)^C, \quad (1)$$

parameterized by the normalization A , the slope B , and the redshift evolution C . Appendix C presents a physical argument for the form of this relation, along with the expected ranges in which the values of the parameters B and C are expected to reside based on self-similar scaling arguments.

Values for the parameters A , B , and C were determined by fitting Eq. 1 to a catalog of $\zeta > 1$ clusters detected in simulated maps, using clusters with mass $M > 2 \times 10^{14} M_\odot h^{-1}$ and in the redshift range $0.3 \leq z \leq 1.2$. This redshift range was chosen to match the SPT sample, while the mass limit was chosen to be as low as possible without the sample being significantly cut off by the $\zeta > 1$ threshold. The best fit was defined as the combination of parameters that minimized the intrinsic fractional scatter around the mean relation.

Figure 3 shows the best-fit scaling relation obtained for our fiducial simulated SZ maps, where $A = 6.01$, $B = 1.31$, and $C = 1.6$. The intrinsic scatter was measured to be 21% (0.21 in $\ln(\zeta)$) and the relation was found to adhere to a power-law well below the limiting mass threshold. Over the three gas model realizations (§4.1), the best fit value of A , B , and the intrinsic scatter were all found to vary by less than 10%, while the values of C predicted by the ‘standard’ and ‘star-formation’ models drop to ~ 1.2 . For maps generated using the electron pressure profile of Arnaud et al. (2010), best-fit values of $A = 6.89$, $B = 1.38$, $C = 0.6$ were found, with a 19% intrinsic scatter. The values of A and B remain within 15% of the fiducial model, although C is significantly lower. Arnaud et al. (2010) measured the pressure profile using a low-redshift ($z < 0.2$) cluster sample and assume that the profile normalization will evolve in a self-similar fashion. The mass dependence of their pressure profile was determined using cluster mass estimates derived from the equation of hydrostatic equilibrium; simulations suggest that this method may underestimate the true mass by 10–20% (Rasia et al. 2004; Meneghetti et al. 2010; Lau et al. 2009). We do not take this effect into account in our simulations – doing so would reduce the value of A by approximately 10%. The Bode et al. (2009) gas model is calibrated against X-ray scaling relations measured from low-redshift cluster samples (Vikhlinin et al. 2006; Sun et al. 2009), but assumes an evolving stellar-mass fraction which may drive the stronger redshift evolution.

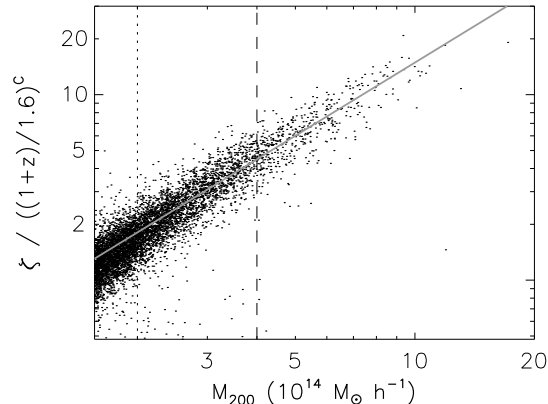


FIG. 3.— Mass-significance relation plotted over clusters identified in simulated maps. The relation was fit to points with $M > 2 \times 10^{14} M_{\odot} h^{-1}$, shown by the dotted line, and across a redshift range $0.3 < z < 1.2$. Simulated clusters outside this redshift range are not included in this plot. The approximate lower mass threshold of the high-redshift end of the SPT sample ($M = 4 \times 10^{14} M_{\odot} h^{-1}$) is shown by the dashed line.

Based on these simulations, priors on the scaling relation parameters (A , B , C , scatter) were adopted, with conservative 1σ Gaussian uncertainties of (30%, 20%, 50%, 20%) about mean values measured from the fiducial simulation model. These large uncertainties in scaling relation parameters are the dominant source of uncertainty in the cosmological analysis (§5) and mass estimation (Appendix C). Furthermore, although the weakest prior is on the redshift evolution, C , it is the uncertainty on the amplitude A that dominates the error budget on the measurement of σ_8 (see §5.4).

It should be noted that at low redshift ($z \lesssim 0.3$), such a power-law scaling relation fails to fully capture the behavior of the CMB-confused selection function. The cosmological analysis below therefore excludes this region during likelihood calculation. The mass estimates presented in Appendix D may be biased low for low-redshift objects, although this effect is expected to be small compared to existing systematic errors.

5. COSMOLOGICAL ANALYSIS

The 2008 SPT cluster catalog is an SZ-detection-significance-limited catalog. Simulated maps were used to calibrate the statistics of the relation between cluster mass and detection significance, as well as the impact of noise-bias and selection effects. This relation was combined with theoretical mass functions to construct estimates of the number density of galaxy clusters as a function of the significance ξ and redshift, to be compared to the SPT catalog. Cosmological information from the SPT cluster catalog was combined with information from existing data sets, providing improved parameter constraints.

5.1. Cosmological Likelihood Evaluation

Evaluation of cosmological models in the context of the SPT catalog requires a theoretical model that is capable of predicting the number density of dark matter halos as a function of both redshift and input cosmology. For a given set of cosmological parameters, the simulation-based mass function of Tinker et al. (2008) was used

in conjunction with matter power spectra computed by CAMB (Lewis et al. 2000) to construct a grid of cluster number densities in the native ξ - z space of the SPT catalog:

- A 2D grid of the number of clusters as a function of redshift and mass was constructed by multiplying the Tinker et al. (2008) mass function by the comoving volume element. The gridding was set to be very fine in both mass and redshift, with $\Delta z = 0.01$ and the mass binning set so that $\Delta \zeta = 0.0025$ (see below). The grids were constructed to extend beyond the sensitivity range of SPT, $0.1 < z < 2.6$ and $1.8 < \zeta < 23$. Extending the upper limits was found not to impact cosmological results, as predicted number counts have dropped to negligible levels above those thresholds.
- The parameterized scaling relation (§4.8) was used to convert the mass for each bin to unbiased significance ζ for assumed values of A , B and C .
- This grid of number counts (in ζ - z space) was convolved with a Gaussian in $\ln(\zeta)$ with width set by the assumed intrinsic scatter in the scaling relation (21% in the fiducial relation).
- The unbiased significance ζ of each bin was converted to an ensemble-averaged significance $\langle \xi \rangle$.
- This grid was convolved with a unit-width Gaussian in ξ to account for noise, with the resulting grid in the native SPT catalog space, ξ - z .
- Each row (fixed ξ) of the ξ - z grid which contained a cluster was convolved with a Gaussian with width set as the redshift uncertainty for that cluster. Photometric redshift uncertainties are given in Table 1, and are described briefly in §2.4 and in detail in High et al. (2009); spectroscopic redshifts were taken to be exact.
- A hard cut in ξ was applied, corresponding to the catalog selection threshold of $\xi \geq 5$.
- An additional cut was applied, requiring $z \geq 0.3$, to avoid low-redshift regions where the power-law scaling relation fails to capture the behavior of the CMB-confused selection function. This cut excludes 3 low-redshift clusters from the cosmological analysis, leaving 18 clusters plus the unconfirmed candidate, whose treatment is described below.

The likelihood ratio for the SPT catalog was then constructed, as outlined in Cash (1979), using the Poisson probability,

$$\mathcal{L} = \prod_{i=1}^N P_i = \prod_{i=1}^N \frac{e_i^{n_i} e^{-e_i}}{n_i!},$$

where the product is across bins in ξ - z space, N is the number of bins, P_i is the Poisson probability in bin i , and e_i and n_i are the fractional expected and integer observed number counts for that bin, respectively.

The unconfirmed candidate was accounted for by simultaneously allowing it to either be at high redshift or

a false detection. Its contribution to the total likelihood was calculated as the union of the likelihoods for $n = 0$ and $n = 1$ within a large $z > 1.0$ bin, the redshift range corresponding to where the optical completeness for this candidate's follow-up deviates from unity.

Ultimately, two sources of mass-observable scatter – the intrinsic scatter in the scaling relation, and the 1σ measurement noise – were included in this analysis, along with redshift errors and systematic uncertainties on scaling relation parameters. Other sources of bias and noise (such as point source contamination, §6.2, and the mass function normalization described below) are thought to be subdominant to these and were disregarded.

While Tinker et al. (2008) claim a very small ($< 5\%$) uncertainty in the mass function normalization, Stanek et al. (2010) have demonstrated that the inclusion of non-gravitational baryon physics in cosmological simulations can modify cluster masses in the range of the SPT sample by $\sim \pm 10\%$ relative to gravity-only hydrodynamical simulations. The large 30% uncertainty on the amplitude A of the scaling relation effectively subsumes such uncertainties in the mass function normalization.

This analysis does not account for the effects of sample variance (Hu & Kravtsov 2003); for the mass and redshift range of the SPT sample, this is not expected to be a problem (Hu & Cohn 2006). The SPT survey fields span of order $100 h^{-1}$ Mpc, where the galaxy cluster correlation function would be expected to be a few percent or less (Bahcall et al. 2003; Estrada et al. 2009). This leads to clustering corrections to the uncertainty on number counts on the order of a few percent or less of the Poisson variance.

5.2. Application to MCMC Chains

The present SPT sample only meaningfully constrains a subset of cosmological parameters, so to explore the cosmological implications of the SPT catalog it is necessary to include information from other experiments. Existing analyses of other cosmological data in the form of Markov Chain Monte Carlo (MCMC) chains provide fully informative priors. These were importance sampled by weighting each set of cosmological parameters in the MCMC chain by the likelihood of the SPT cluster catalog given that set of parameters.

In this analysis, four MCMC chains were used to explore constraints on parameters: the first two use only the 7-year data set from the WMAP experiment to explore the standard spatially flat Λ CDM and w CDM cosmologies, while the third explores w CDM while adding data from baryon acoustic oscillations (BAO) (Percival et al. 2010) and supernovae (SNe) (Hicken et al. 2009). These three chains were taken from the official WMAP analysis³ (Komatsu et al. 2010). The fourth chain was computed by L10 and allows for a direct comparison with that work. It explores a spatially flat Λ CDM parameter space based on the ‘‘CMBall’’ data set: WMAP 5-year + QUaD (Brown et al. 2009) + ACBAR (Reichardt et al. 2009) + SPT (power spectrum measurements with A_{SZ} as a free parameter; L10).

Figure 4 shows the number density of clusters in the SPT catalog, plotted over theoretical predictions calculated using the method described in §5.1, for 100 ran-

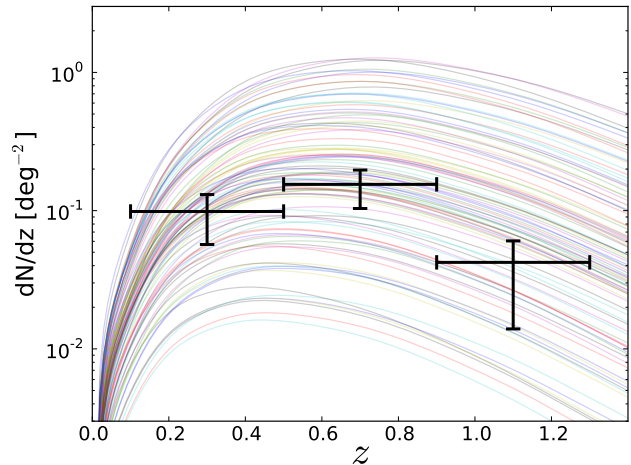


FIG. 4.— The SPT catalog, binned into 3 redshift bins ($z=0.1-0.5$, $0.5-0.9$, $0.9-1.3$), with number counts derived from 100 randomly selected points in the WMAP7 w CDM MCMC chain overplotted. The SPT data are well covered by the chain and provide improved constraining power. The unconfirmed candidate is not included in this plot, and the binning is much coarser for display purposes than that used in the likelihood calculation (§5.1).

dom positions in the WMAP7-only MCMC chain. The SPT data are adequately described by many cosmological models that are allowed by this data set, and the MCMC chains are well-sampled within the region of high probability.

Uncertainties in the scaling relation parameters were accounted for by marginalizing over them: at each step in the chain, the likelihood was maximized across A , B , C and scatter, subject to the priors applied to each parameter, using a Newton-Raphson method. The parameter values selected in this way at the highest likelihood point in each MCMC chain are given in Table C1. The fiducial values of B and the scatter appear consistent with those preferred by the chains, while the preferred values of the normalization A and redshift evolution C are both approximately 10% lower than their fiducial values.

This weaker-than-fiducial redshift evolution could come from a variety of sources, and is consistent with other simulated models, e.g., the ‘standard’ and ‘star-formation’ models, see §4.8. Uncertainties in the redshift evolution are not a significant source of error in this analysis: recovered parameter values and uncertainties (§5.3) are found to be insignificantly affected by widely varying priors on C .

5.3. Cosmological Parameter Constraints

The resulting constraints on σ_8 and w are given for all chains in Table 2. The parameter best constrained by the SPT cluster catalog is σ_8 . CMB power spectrum measurements alone have a large degeneracy between the dark energy equation of state, w , and σ_8 . Figure 5 shows this degeneracy, along with the added constraints from the SPT cluster catalog. Including the cluster results tightens the σ_8 contours and leads to an improved constraint on w . This is a growth-based determination of the dark energy equation of state, and is therefore complementary to dark energy measurements based on distances, such as those based on SNe and BAO.

When combined with the w CDM WMAP7 chain, the

³ Chains available at <http://lambda.gsfc.nasa.gov>

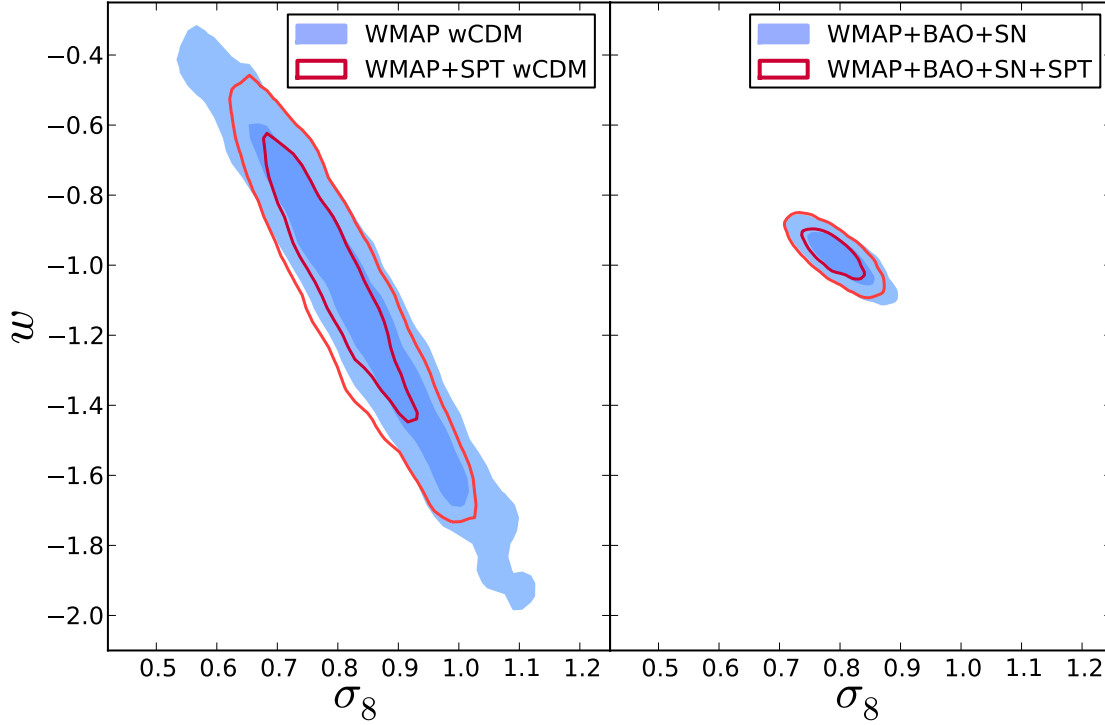


FIG. 5.— Likelihood contour plot of w versus σ_8 showing 1σ and 2σ contours for several data sets. The left panel shows the constraints from WMAP7 alone (blue) and with the SPT cluster catalog included (red). The right panel shows the full cosmological data set of WMAP7+SN+BAO (blue), and this plus the SPT catalog (red). The ability to constrain cosmological parameters is severely impacted by the uncertainties in the mass scaling relation, though some increase in precision is still evident.

TABLE 2
COSMOLOGICAL PARAMETER CONSTRAINTS

Chain	σ_8	w
Λ CDM WMAP7	0.801 ± 0.030	-1
Λ CDM WMAP7+SPT	0.791 ± 0.027	-1
Λ CDM CMBall	0.794 ± 0.029	-1
Λ CDM CMBall+SPT	0.788 ± 0.026	-1
wCDM WMAP7	0.832 ± 0.134	-1.118 ± 0.394
wCDM WMAP7+SPT	0.810 ± 0.090	-1.066 ± 0.288
wCDM WMAP7+BAO+SNe	0.802 ± 0.038	-0.980 ± 0.053
wCDM WMAP7+BAO+SNe+SPT	0.790 ± 0.034	-0.968 ± 0.049

NOTE. — Mean values and symmetrized 1σ range for σ_8 and w , as found from each of the four data sets considered, shown with and without the weighting by likelihoods derived from the SPT cluster catalog. The parameter best constrained by the SPT cluster catalog is σ_8 . CMB power spectrum measurements alone have a large degeneracy between the dark energy equation of state, w , and σ_8 . Adding the SPT cluster catalog breaks this degeneracy and leads to an improved constraint on w . The SPT catalog has negligible effect on other parameters in these chains ($\Omega_b h^2$, $\Omega_c h^2$, H_0 , τ and n_s).

SPT data provide roughly a factor of 1.5 improvement in the precision of σ_8 and w , finding 0.81 ± 0.09 and -1.07 ± 0.29 , respectively. Including data from BAO and SNe, these constraints tighten to $\sigma_8 = 0.79 \pm 0.03$ and $w = -0.97 \pm 0.05$.

The dominant sources of uncertainty limiting these constraints are the Poisson error due to the relatively modest size of the current catalog and the uncertainty in the normalization A of the mass scaling relation. With weak-lensing- and X-ray-derived mass estimates of SPT clusters, along with an order of magnitude larger sample expected from the full survey, cosmological constraints from the SPT galaxy cluster survey will markedly improve.

5.4. Amplitude of the SZ Effect

The value of the normalization parameter A (which can be thought of as an “SZ amplitude”) preferred by the likelihood analysis was found to be lower than the fiducial value, as shown in Figure 6. The prior assumed on this parameter is sufficiently large that it is not a highly significant shift; however, in light of the recent report by L10 of lower-than-expected SZ flux, it is worth addressing. The SPT cluster catalog results are complementary to the the results of the power spectrum analysis, in that the majority of the SZ power at the angular scales probed by L10 comes from clusters below the mass threshold of the cluster catalog.

Figure 6 shows that the amplitude A is strongly degenerate with σ_8 . The constraints provided by the SPT cluster catalog indicate either a value of σ_8 that is at the low end of the CMB-allowed distribution (or equivalently an erroneously high mass function normalization), or an over-prediction of SZ flux by the fiducial simulations. If the fiducial amplitude is assumed, the best-fit σ_8 drops from the WMAP5+CMBall value of 0.794 ± 0.029 to 0.775 ± 0.015 . This value is anomalously low compared to recent results (e.g. Vikhlinin et al. 2009; Mantz et al. 2010), and in slight tension with the results of the power spectrum analysis of L10, where a still lower value of $\sigma_8 = 0.746 \pm 0.017$ was obtained for similar simulation models.⁴ The SZ amplitude parameter used in L10, A_{sz} , is roughly analogous to A^2 in the current notation. When including the expected contribution from homogeneous reionization, L10 found $A_{sz} = 0.42 \pm 0.21$, in mild tension (at the $\sim 1\sigma$ level) with the marginalized value of $(A/A_{fid})^2 = 0.79 \pm 0.30$ found in this analysis.

The fiducial simulations in this work use the semi-analytic gas model of Bode et al. (2007, 2009), which is calibrated against low-redshift ($z < 0.25$) X-ray observations but has not previously been compared to higher redshift systems. One interpretation of these results is that this model may over-predict the thermal electron pressure in high-redshift ($z > 0.3$) systems; this is not in conflict with the low-redshift calibration of the model and suggests a weaker redshift evolution in the SZ signal than predicted by the model. Alternately, a combination of mass function normalization and point source contamination could potentially account for the difference.

⁴ The fiducial thermal SZ simulation model used in this paper predicts a power spectrum that is in very close agreement with the fiducial model of L10, which was measured from the simulations of Sehgal et al. (2010).

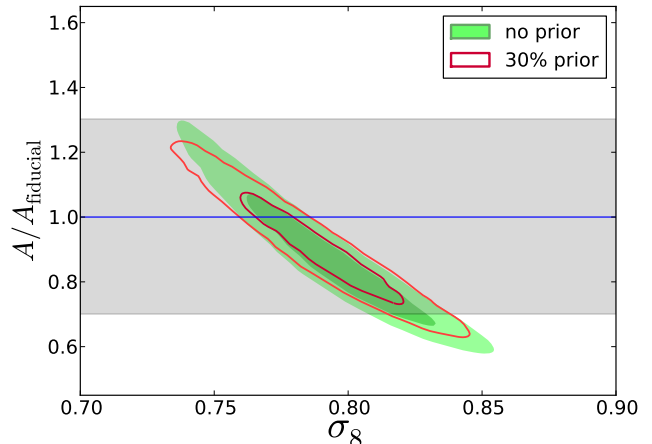


FIG. 6.— Degeneracy between σ_8 and SZ scaling relation amplitude A , plotted without prior (green) and with a 30% Gaussian prior (red) on A , for the Λ CDM WMAP5+CMBall MCMC chain. The Gaussian prior is shown ($\pm 1\sigma$) by the gray band, with the fiducial relation amplitude shown by the blue line. This figure is analogous to Fig. 9 of L10, although that work dealt with SZ power, which is roughly proportional to the square of the amplitude being considered here. The prior is slightly higher than the preferred value; these results suggest that simulations may over-estimate the SZ flux in the high-mass, high-redshift systems contained in this catalog.

6. SOURCES OF SYSTEMATIC UNCERTAINTIES

There are several systematic effects that might affect the utility of the SPT cluster sample. For example, there remains large uncertainty in the mapping between detection significance and cluster mass. It is also possible that strong correlations (or anti-correlations) between galaxy clusters and mm-bright point sources are significant. We address these issues in this section.

6.1. Relation between SZ signal and Mass

Theoretical arguments (Barbosa et al. 1996; Holder & Carlstrom 2001; Motl et al. 2005) suggest that the SZ flux of galaxy clusters is relatively well understood. However, there is very little high-precision empirical evidence to confirm these arguments, and there are physical mechanisms that could lead to suppressed SZ flux, such as non-thermal pressure support from turbulence (Lau et al. 2009) or non-equilibrium between protons and electrons (Fox & Loeb 1997; Rudd & Nagai 2009).

Cluster SZ mass proxies (such as Y and y_0 , the integrated SZ flux and amplitude of the SZ decrement, respectively) depend linearly on the gas fraction and the gas temperature. There remain theoretical and observational uncertainties in both of these quantities. Estimates of gas fractions for individual clusters can disagree by nearly 20% (e.g., Allen et al. 2008; Vikhlinin et al. 2006), while theoretical and observed estimates of the mass-temperature relation currently agree at the level of 10-20% (Nagai et al. 2007). Adding these in quadrature leads to uncertainties slightly below our assumed prior uncertainty of 30%.

With the number counts as a function of mass, $dN/d\ln M$, scaling as M^{-2} or M^{-3} for typical SPT clusters (Shaw et al. 2010a), a 10% offset in mass would lead to a 20-30% shift in the number of galaxy clusters. With

a catalog of 22 clusters, counting statistics lead to an uncertainty of at least 20%. Therefore, systematic offsets in the mass scale of order 10% will have a significant effect on cosmological constraints, and the current 30% prior on A will dominate Poisson errors.

A follow-up campaign using optical and X-ray observations will buttress our current theory/simulation-driven understanding of the SPT SZ-selected galaxy cluster catalog.

6.2. Clusters Obscured by Point Sources

The sky density of bright point sources at 150 GHz is low enough — on the order of 1 deg^{-2} (Vieira et al. 2010) — that the probability of a galaxy cluster being missed due to a chance superposition with a bright source is negligible. However, sources associated with clusters will preferentially fill in cluster SZ decrements. Characterizing the contamination of cluster SZ measurements by member galaxies will be necessary to realize the full potential of the upcoming much larger SPT cluster catalog, but the systematic uncertainty predicted here and in the literature is well below the statistical precision of the current sample; it is disregarded in the current cosmological analysis (§5).

6.2.1. Dusty Source Contamination

Star formation is expected to be suppressed in cluster environments (e.g., Hashimoto et al. 1998). Bai et al. (2007) measure the abundance of infrared-luminous star-forming galaxies in a massive ($\gtrsim 10^{15} M_{\odot}$) cluster at $z = 0.8$ to be far lower relative to the field abundance than a simple mass scaling would predict: the cluster volume that is hundreds of times overdense in mass is only 20 times overdense in infrared luminosity. A sphere at $z = 1$ with a 1 Mpc radius and infrared luminosity that is 20 times larger than the field would produce $< 0.1 \text{ mJy}$ of emission at 150 GHz, according to the sub-mm luminosity measurements of BLAST (Pascale et al. 2009) (Pascale et al. 2009). Even if the IR overdensity evolves strongly with mass and redshift, we can expect $\ll 1 \text{ mJy}$ of contamination for the highest-redshift ($z \sim 1$) clusters at the SPT mass threshold. This corresponds to $\ll 10\%$ of the cluster SZ signal, which is far less than the uncertainty in the normalization of cluster masses presented in this work.

Additionally, Keisler (2010, in prep.) measures the average $100 \mu\text{m}$ flux of cluster members from a sample of clusters at $\langle z \rangle = 0.2$ and with masses similar to those selected by SPT and, after extrapolating to 150 GHz and allowing for strong redshift evolution in the infrared luminosity function, constrains this contamination to be less than 10% of the cluster SZ signal. Again, this level of contamination is subdominant to the uncertainty in the normalization of cluster masses presented in this work.

6.2.2. Gravitational Lensing

Galaxy clusters can gravitationally lens sources located behind them. Because gravitational lensing conserves surface brightness, this process cannot alter the mean flux due to the background sources when averaged over many clusters. The background of sources is composed of both overdensities and underdensities, leading to both positive and negative fluctuations, relative to the mean, which will be gravitationally lensed.

We do not explicitly account for this effect in this work. The unlensed fluctuating background of sources at 150 GHz is expected to be small (Hall et al. 2010) compared to both the experimental noise and intrinsic scatter on the mass scaling relation, and lensing only marginally increases the noise associated with these background sources (Lima et al. 2010). Within the context of the cosmological analysis, this additional noise term is expected to be small compared to the intrinsic scatter on the mass scaling relation.

6.2.3. Radio Source Contamination

Galaxy clusters are known to host radio sources, but these correlated sources are not expected to be a major contaminant at 150 GHz. Calculations (Lin et al. 2009) and explicit simulations (Sehgal et al. 2010) demonstrate that, even taking into account the expected correlation between clusters and radio sources, these sources are not expected to significantly affect the SZ flux in more than 1% percent of galaxy clusters above $2 \times 10^{14} M_{\odot}$ at a redshift of $z \sim 0.5$ (where “significantly” here means at the $\geq 20\%$ level).

Simulations were also performed using knowledge of the radio source population at 150 GHz from Vieira et al. (2010) and the cluster profiles that maximize the significance for the SPT clusters presented here. Each profile between $r_{\text{core}} = 0.25'$ and $r_{\text{core}} = 1.5'$ (a range which encompasses all of the optically confirmed clusters in Table 1) was scaled so that the filtered version of that profile would result in a $\xi = 5$ detection in the 2008 SPT maps. Point sources of a given flux were then added at a given radius from the profile center. These point-source-contaminated profiles were then convolved with the transfer function, the matched filter was applied, and the resulting central value was compared to the central value of the filter-convolved, uncontaminated profile. Clusters were found to suffer a systematic $\Delta\xi = 1$ reduction in significance from a 2 mJy (5 mJy) source at $0.5' (1')$ from the profile center. This effect is nearly independent of core radius in the range of core radii probed.

The Vieira et al. (2010) radio source counts at 150 GHz indicate roughly 1.5 per deg^2 above 5 mJy, while the de Zotti et al. (2005) 150 GHz model predicts roughly 3 radio sources per deg^2 above 2 mJy.⁵ If there were no correlation between clusters and radio sources, the clusters contained in the SPT catalog should have a 0.14% (0.03%) chance of incurring an error of $\Delta\xi \geq 1$ from a $\geq 5 \text{ mJy}$ ($2 - 5 \text{ mJy}$) source.

Furthermore, using 30 GHz observations of a sample of clusters ranging from $0.14 < z < 1.0$, Coble et al. (2007) find the probability of finding a radio source near a cluster to be $8.9^{+4.3}_{-2.8}$ ($3.3^{+4.1}_{-1.8}$) times the background rate when using a $0.5' (5')$ radius. From these results, it can be estimated that roughly 1% of SPT-detected clusters would suffer an error of $\Delta\xi \geq 1$ from radio source contamination. This is in very close agreement with the predictions from Lin et al. (2009) and Sehgal et al. (2010).

7. DISCUSSION

⁵ The Vieira et al. (2010) counts do not cover a low enough flux range to predict counts at 2 mJy, but the de Zotti et al. (2005) model is consistent with the Vieira et al. (2010) counts at all fluxes above 5 mJy, so counts from this model can confidently be extrapolated down a factor of 2.5 in flux.

We have presented the first cosmologically significant SZ-selected galaxy cluster catalog, characterized the selection function, and performed a preliminary cosmological analysis to both demonstrate the general consistency of the catalog with current understanding of cosmology and provide improved constraints on cosmological parameters. This is an important step toward exploiting the potential of SZ-selected galaxy clusters as a powerful cosmological tool.

Using single-frequency data taken in 2008 with SPT, a total of 22 candidates were identified, all but one of which were optically confirmed as galaxy clusters (High et al. 2010). Of these 21 clusters, three were previously known from optical and/or X-ray surveys, three were new SPT detections reported in S09, three were first identified from BCS data by Menanteau et al. (2010), and 12 are new discoveries.

Simulations were used to calibrate the selection function of the survey and measure a scaling between SPT detection significance and mass. These simulations indicate that SZ detection significance traces mass with little ($\sim 20\%$) intrinsic scatter, making SZ surveys well suited to selecting mass-limited catalogs of galaxy clusters.

As a demonstration of the constraining power of the survey, the SPT cluster catalog was used to refine estimates of cosmological parameters, including the dark energy equation of state, w , and the normalization of the matter power spectrum on small scales, σ_8 . Using Λ CDM MCMC chains derived from the WMAP 7-year data combined with the SPT cluster catalog, the best-fit values were $w = -1.07 \pm 0.29$ and $\sigma_8 = 0.81 \pm 0.09$, a factor of roughly 1.5 improvement in precision compared to the WMAP7 constraints alone. When combined with other cosmological data sets (baryon acoustic oscillations and supernovae), the SPT cluster catalog improves precision on these parameters by $\sim 10\%$.

These results can be compared to those of Vikhlinin et al. (2009) and Mantz et al. (2010), who performed a similar analysis using large samples of clusters drawn from X-ray surveys. The SPT results are less precise: in combination with various cosmological data sets, Vikhlinin et al. (2009) find nearly 4 times tighter constraints on σ_8 , while Mantz et al. (2010) are more precise by nearly a factor of 2. This is not surprising: both X-ray analyses had significantly larger cluster samples and smaller stated uncertainty in the mass scaling relation. The weaker parameter constraints found from the SPT cluster catalog are a direct result of uncertainties in the mass scaling relation, which derive from uncertainties modeling intra-cluster physics.

The fiducial thermal SZ simulation model assumed here was shown to produce some tension between the analysis presented here and contemporary cosmological results. This may be explained by a variety of factors. The value of σ_8 may be lower than currently favored, or equivalently the normalization of the Tinker et al. (2008) mass function may be erroneously high. Alternatively, current simulations, while reproducing observed low-redshift X-ray observations, may over-estimate SZ flux in higher redshift systems, implying missing physics in the semi-analytic gas modeling (for example, a non-negligible amount of non-thermal pressure support at higher redshifts, Shaw et al. 2010b). The observed SZ signal could potentially be contaminated by an in-

creasing incidence of point-source emission at high redshift although the arguments presented in §6.2 suggest point-source contamination is unlikely to be wholly responsible. L10 also found lower-than-anticipated power from the SPT measurement of the SZ power spectrum, consistent with many of these scenarios. A concerted, multi-wavelength program aimed at studying high redshift clusters should help to resolve these issues.

The SPT catalog presented here is based on less than 1/3 of the current data and roughly 1/10 of the full SPT survey. The large multifrequency SPT survey, combined with X-ray and/or weak lensing mass estimates of a subsample of SZ-selected galaxy clusters, should allow an order of magnitude improvement in the precision of σ_8 and w measurements.

The SPT team gratefully acknowledges the contributions to the design and construction of the telescope by S. Busetti, E. Chauvin, T. Hughes, P. Huntley, and E. Nichols and his team of iron workers. We also thank the National Science Foundation (NSF) Office of Polar Programs, the United States Antarctic Program and the Raytheon Polar Services Company for their support of the project. We are grateful for professional support from the staff of the South Pole station. We thank H.-M. Cho, T. Lanting, J. Leong, W. Lu, M. Runyan, D. Schwan, M. Sharp, and C. Greer for their early contributions to the SPT project and J. Joseph and C. Vu for their contributions to the electronics. We acknowledge S. Alam, W. Barkhouse, S. Bhattacharya, L. Buckley-Greer, S. Hansen, H. Lin, Y-T Lin, C. Smith and D. Tucker for their contribution to BCS data acquisition, and we acknowledge the DESDM team, which has developed the tools we used to process and calibrate the BCS data.

We acknowledge the use of the Legacy Archive for Microwave Background Data Analysis (LAMBDA). Support for LAMBDA is provided by the NASA Office of Space Science. This research was facilitated in part by allocations of time on the COSMOS supercomputer at DAMTP in Cambridge, a UK-CCC facility supported by HEFCE and PPARC. This work is based in part on observations obtained at the Cerro Tololo Inter-American Observatory, and the Las Campanas Observatory. CTIO is operated by the Association of Universities for Research in Astronomy (AURA), Inc., under cooperative agreement with the National Science Foundation (NSF).

The South Pole Telescope is supported by the National Science Foundation through grants ANT-0638937 and ANT-0130612. Partial support is also provided by the NSF Physics Frontier Center grant PHY-0114422 to the Kavli Institute of Cosmological Physics at the University of Chicago, the Kavli Foundation and the Gordon and Betty Moore Foundation. This research used resources of the National Energy Research Scientific Computing Center, which is supported by the Office of Science of the U.S. Department of Energy under Contract No. DE-AC02-05CH11231. This work is supported in part by the Director, Office of Science, Office of High Energy Physics, of the U.S. Department of Energy under Contract No. DE-AC02-05CH11231. The McGill group acknowledges funding from the National Sciences and Engineering Research Council of Canada, the Que-

bec Fonds de recherche sur la nature et les technologies, and the Canadian Institute for Advanced Research. Partial support was provided by NSF grant MRI-0723073. The following individuals acknowledge additional support: A. Loehr and B. Stalder from the Brinson Foundation, B. Benson and K. Schaffer from KICP Fellowships, J. McMahon from a Fermi Fellowship, R. Foley from

a Clay Fellowship, D. Marrone from Hubble Fellowship grant HF-51259.01-A, M. Brodwin from the Keck Foundation, Z. Staniszewski from a GAAN Fellowship, and A.T. Lee from the Miller Institute for Basic Research in Science, University of California Berkeley.

Facilities: Blanco (MOSAIC II), Magellan:Baade (IMACS), Magellan:Clay (LDSS2)

REFERENCES

- Abell, G. O., Corwin, Jr., H. G., & Olowin, R. P. 1989, *ApJS*, 70, 1
- Allen, S. W., Rapetti, D. A., Schmidt, R. W., Ebeling, H., Morris, R. G., & Fabian, A. C. 2008, *MNRAS*, 383, 879
- Arnaud, M., Pratt, G. W., Piffaretti, R., Böhringer, H., Croston, J. H., & Pointecouteau, E. 2010, *A&A*, 517, A92+
- Bahcall, N. A., Dong, F., Hao, L., Bode, P., Annis, J., Gunn, J. E., & Schneider, D. P. 2003, *ApJ*, 599, 814
- Bai, L., et al. 2007, *ApJ*, 664, 181
- Barbosa, D., Bartlett, J., Blanchard, A., & Oukbir, J. 1996, *A&A*, 314, 13
- Battye, R. A., & Weller, J. 2003, *Phys. Rev. D*, 68, 083506
- Bertin, E., & Arnouts, S. 1996, *A&AS*, 117, 393
- Birkinshaw, M. 1999, *Physics Reports*, 310, 97
- Bode, P., Ostriker, J. P., & Vikhlinin, A. 2009, *ApJ*, 700, 989
- Bode, P., Ostriker, J. P., Weller, J., & Shaw, L. 2007, *ApJ*, 663, 139
- Böhringer, H., et al. 2004, *A&A*, 425, 367
- Brown, M. L., et al. 2009, *ApJ*, 705, 978
- Bruzual, G., & Charlot, S. 2003, *MNRAS*, 344, 1000
- Carlstrom, J. E., et al. 2009, submitted to *PASP*, arXiv:0907.4445
- Carlstrom, J. E., Holder, G. P., & Reese, E. D. 2002, *ARA&A*, 40, 643
- Cash, W. 1979, *ApJ*, 228, 939
- Coble, K., et al. 2007, *AJ*, 134, 897
- de Zotti, G., Ricci, R., Mesa, D., Silva, L., Mazzotta, P., Toffolatti, L., & González-Nuevo, J. 2005, *A&A*, 431, 893
- Duffy, A. R., Schaye, J., Kay, S. T., & Dalla Vecchia, C. 2008, *MNRAS*, 390, L64
- Dunkley, J., et al. 2009, *ApJS*, 180, 306
- Estrada, J., Sefusatti, E., & Frieman, J. A. 2009, *ApJ*, 692, 265
- Fowler, J. W., et al. 2007, *Appl. Opt.*, 46, 3444
- Fox, D., & Loeb, A. 1997, *ApJ*, 491, 459
- Granato, G. L., De Zotti, G., Silva, L., Bressan, A., & Danese, L. 2004, *ApJ*, 600, 580
- Haehnelt, M. G., & Tegmark, M. 1996, *MNRAS*, 279, 545+
- Haiman, Z., Mohr, J. J., & Holder, G. P. 2001, *ApJ*, 553, 545
- Hall, N. R., et al. 2010, *ApJ*, 718, 632, arXiv:0912.4315
- Hashimoto, Y., Oemler, Jr., A., Lin, H., & Tucker, D. L. 1998, *ApJ*, 499, 589
- Herranz, D., Sanz, J. L., Barreiro, R. B., & Martínez-González, E. 2002a, *ApJ*, 580, 610
- Herranz, D., Sanz, J. L., Hobson, M. P., Barreiro, R. B., Diego, J. M., Martínez-González, E., & Lasenby, A. N. 2002b, *MNRAS*, 336, 1057
- Hicken, M., Wood-Vasey, W. M., Blondin, S., Challis, P., Jha, S., Kelly, P. L., Rest, A., & Kirshner, R. P. 2009, *ApJ*, 700, 1097
- High, F. W., et al. 2010, submitted to *ApJ*, arXiv:1003.0005
- High, F. W., Stubbs, C. W., Rest, A., Stalder, B., & Challis, P. 2009, *AJ*, 138, 110
- Hinshaw, G., et al. 2009, *ApJS*, 180, 225
- Holder, G., & Carlstrom, J. 1999, in *Microwave Foregrounds*, ed. A. de Oliveira-Costa & M. Tegmark (San Francisco: ASP-astro-ph/9904220)
- Holder, G., Haiman, Z., & Mohr, J. J. 2001, *ApJ*, 560, L111
- Holder, G. P., & Carlstrom, J. E. 2001, *ApJ*, 558, 515, astro-ph/0105229
- Hu, W., & Cohn, J. D. 2006, *Phys. Rev. D*, 73, 067301
- Hu, W., & Kravtsov, A. V. 2003, *ApJ*, 584, 702
- Jones, D. H., Saunders, W., Read, M., & Colless, M. 2005, *Publications of the Astronomical Society of Australia*, 22, 277
- Keisler, R. 2010, In Preparation
- Komatsu, E., et al. 2010, *ArXiv e-prints*, 1001.4538
- Larson, D., et al. 2010, *ArXiv e-prints*, 1001.4635
- Lau, E. T., Kravtsov, A. V., & Nagai, D. 2009, *ApJ*, 705, 1129
- Lewis, A., Challinor, A., & Lasenby, A. 2000, *ApJ*, 538, 473
- Lewis, A., Challinor, A., & Turok, N. 2002, *Phys. Rev. D*, 65, 023505, astro-ph/0106536
- Lima, M., & Hu, W. 2007, *Phys. Rev. D*, 76, 123013
- Lima, M., Jain, B., & Devlin, M. 2010, *MNRAS*, 406, 2352
- Lin, Y., Partridge, B., Pober, J. C., Boucheffry, K. E., Burke, S., Klein, J. N., Coish, J. W., & Hufferberger, K. M. 2009, *ApJ*, 694, 992
- Lueker, M., et al. 2010, *ApJ*, 719, 1045
- Mantz, A., Allen, S. W., Rapetti, D., & Ebeling, H. 2010, *MNRAS*, 406, 1759
- Melin, J.-B., Bartlett, J. G., & Delabrouille, J. 2006, *A&A*, 459, 341
- Menanteau, F., et al. 2010, *ArXiv e-prints*, 1002.2226
- Meneghetti, M., Rasia, E., Merten, J., Bellagamba, F., Ettori, S., Mazzotta, P., Dolag, K., & Marri, S. 2010, *A&A*, 514, A93+
- Molnar, S. M., Haiman, Z., Birkinshaw, M., & Mushotzky, R. F. 2004, *ApJ*, 601, 22
- Motl, P. M., Hallman, E. J., Burns, J. O., & Norman, M. L. 2005, *ApJ*, 623, L63
- Murphy, T., et al. 2010, *MNRAS*, 402, 2403
- Nagai, D., Kravtsov, A. V., & Vikhlinin, A. 2007, *ApJ*, 668, 1
- Negrello, M., Perrotta, F., González-Nuevo, J., Silva, L., de Zotti, G., Granato, G. L., Baccigalupi, C., & Danese, L. 2007, *MNRAS*, 377, 1557
- Ngew, C. C., Mohr, J., Zenteno, A., Data Management, D., BCS, & SPT Collaborations. 2009, in *Bulletin of the American Astronomical Society*, Vol. 41, *Bulletin of the American Astronomical Society*, 335+
- Osip, D. J., Floyd, D., & Covarrubias, R. 2008, in *Society of Photo-Optical Instrumentation Engineers (SPIE) Conference Series*, Vol. 7014, *Society of Photo-Optical Instrumentation Engineers (SPIE) Conference Series*, 70140A–70140A–10
- Pascale, E., et al. 2009, *ApJ*, 707, 1740
- Percival, W. J., et al. 2010, *MNRAS*, 401, 2148
- Perlmutter, S., et al. 1999, *ApJ*, 517, 565, astro-ph/9812133
- Plagge, T., et al. 2010, *ApJ*, 716, 1118
- Rasia, E., Tormen, G., & Moscardini, L. 2004, *MNRAS*, 351, 237
- Reichardt, C. L., et al. 2009, *ApJ*, 694, 1200
- Rudd, D. H., & Nagai, D. 2009, *ApJ*, 701, L16
- Schmidt, B. P., et al. 1998, *ApJ*, 507, 46
- Sehgal, N., Bode, P., Das, S., Hernandez-Monteagudo, C., Hufferberger, K., Lin, Y., Ostriker, J. P., & Trac, H. 2010, *ApJ*, 709, 920
- Shaw, L. D., Holder, G. P., & Dudley, J. 2010a, *ApJ*, 716, 281
- Shaw, L. D., Nagai, D., Bhattacharya, S., & Lau, E. T. 2010b, *ArXiv e-prints*, 1006.1945, arXiv:1006.1945
- Shaw, L. D., Zahn, O., Holder, G. P., & Doré, O. 2009, *ApJ*, 702, 368
- Stanek, R., Rasia, E., Evrard, A. E., Pearce, F., & Gazzola, L. 2010, *ApJ*, 715, 1508
- Staniszewski, Z., et al. 2009, *ApJ*, 701, 32
- Sun, M., Voit, G. M., Donahue, M., Jones, C., Forman, W., & Vikhlinin, A. 2009, *ApJ*, 693, 1142
- Sunyaev, R. A., & Zel'dovich, Y. B. 1972, *Comments on Astrophysics and Space Physics*, 4, 173
- Tinker, J., Kravtsov, A. V., Klypin, A., Abazajian, K., Warren, M., Yepes, G., Gottlöber, S., & Holz, D. E. 2008, *ApJ*, 688, 709
- Vieira, J. D., et al. 2010, *ApJ*, 719, 763
- Vikhlinin, A., Kravtsov, A., Forman, W., Jones, C., Markevitch, M., Murray, S. S., & Van Speybroeck, L. 2006, *ApJ*, 640, 691
- Vikhlinin, A., et al. 2009, *ApJ*, 692, 1060
- Voges, W., et al. 1999, *A&A*, 349, 389
- . 2000, *VizieR Online Data Catalog*, 9029, 0
- Wang, L., & Steinhardt, P. J. 1998, *ApJ*, 508, 483
- Wang, S., Khoury, J., Haiman, Z., & May, M. 2004, *Phys. Rev. D*, 70, 123008

APPENDIX

A. THUMBNAIL IMAGES OF CLUSTER SZ DECREMENTS

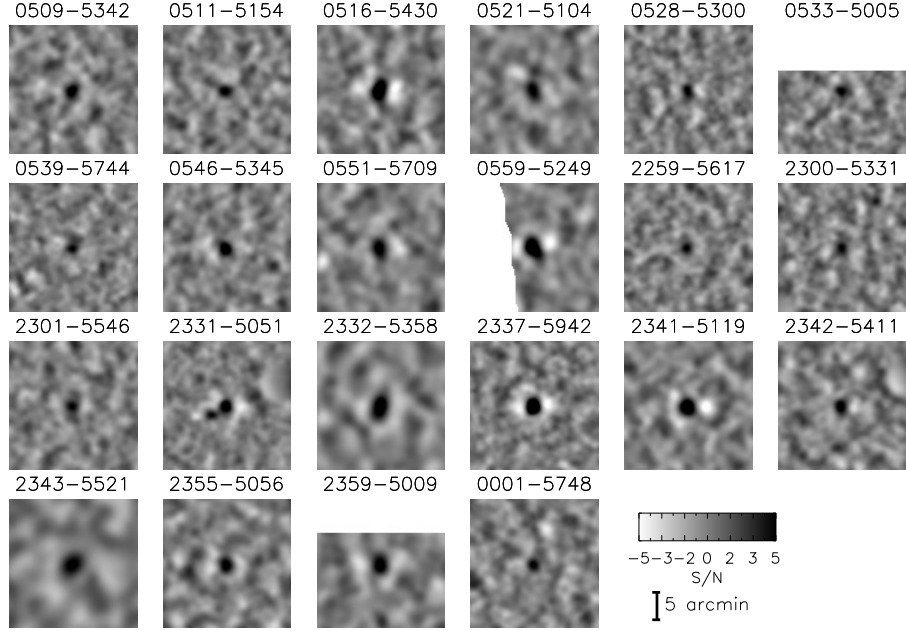


FIG. A1.— Thumbnail cutouts of filtered maps, $25' \times 25'$, of the highest significance filter scale for each cluster, centered on the cluster position. The color scale and spatial extent of all maps here are the same, and the irregular shape of some images shows the edge of the masked (even coverage) map. The large blur in the upper right of SPT-CL J2331-5051 is a point source mask.

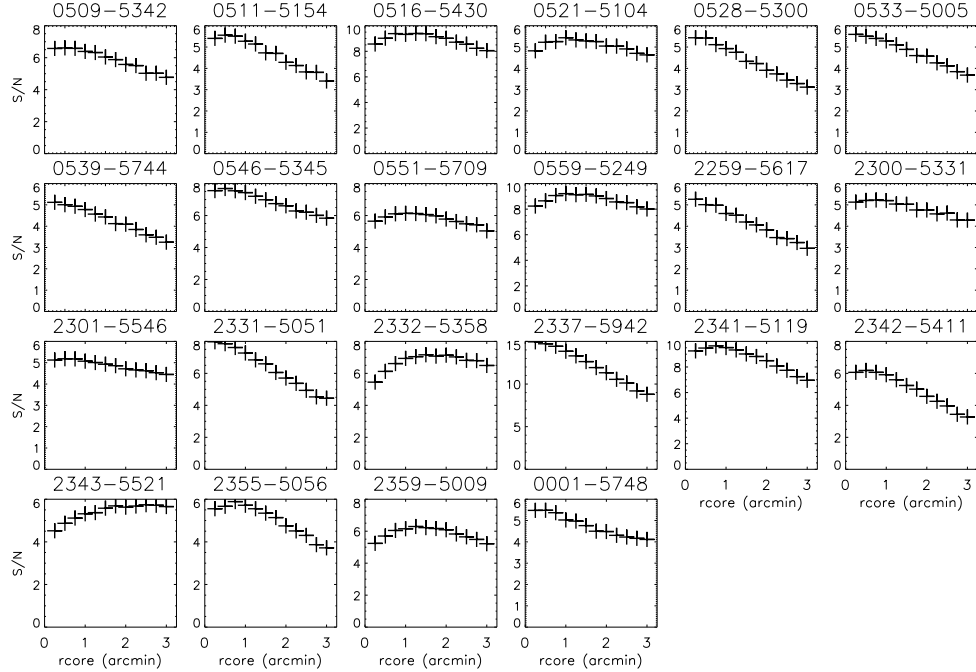


FIG. A2.— The measured significance across filter scales for all clusters. The maximum value of each curve gives ξ for that candidate. The significance axes have been allowed to float for each panel. Adjacent points are highly correlated, and as discussed in §3.2, the best-fit θ_c is poorly constrained.

B. UNBIASED SIGNIFICANCE ζ

The freedom to maximize the SPT significance ξ across three parameters (R.A., decl., and θ_c) in the presence of a noise field will tend to raise the amplitude of the observed peak. That is, the ensemble average of ξ across many noise realizations, $\langle \xi \rangle$, will be boosted by some amount as compared to the unbiased significance ζ , which is measured without these degrees of freedom.

We can consider the SPT significance ξ as analogous to a χ^2 of the best-fit model relative to zero signal, with the signal to noise being comparable to $\sqrt{\chi^2}$. By allowing three degrees of freedom in a usual χ^2 fit, we expect that the minimum χ^2 will typically be smaller than the corresponding one for a fit with no degrees of freedom, i.e., at the true location using the true filter size. The typical difference is simply the number of fit parameters, in our case three: $\langle \xi \rangle^2 - \zeta^2 = 3$.

We test the relation on simulated data, adding 25 different realizations of each noise term (CMB, point sources, instrumental and atmospheric) to the same SZ sky, and explicitly measuring $\langle \xi \rangle$ for many simulated clusters in these maps. We next simulate and measure ζ for the same patch of sky and compare the two measures of significance. The results of these simulations are shown in Figure B1, and are consistent with the hypothesized relation with $\chi^2 = 27$ for 23 degrees of freedom.

We adopt this relation for the cosmological analysis and mass estimation,

$$\zeta \approx \sqrt{\langle \xi \rangle^2 - 3},$$

and find that any residual behavior not modeled by this relation is small enough to be well sub-dominant to uncertainties on the scaling relation amplitude A and Poisson noise within the catalog. Within the SPT catalog this is a small effect: for $\langle \xi \rangle = 5(10)$ objects, the difference between ζ and $\langle \xi \rangle$ is 6%(1%).

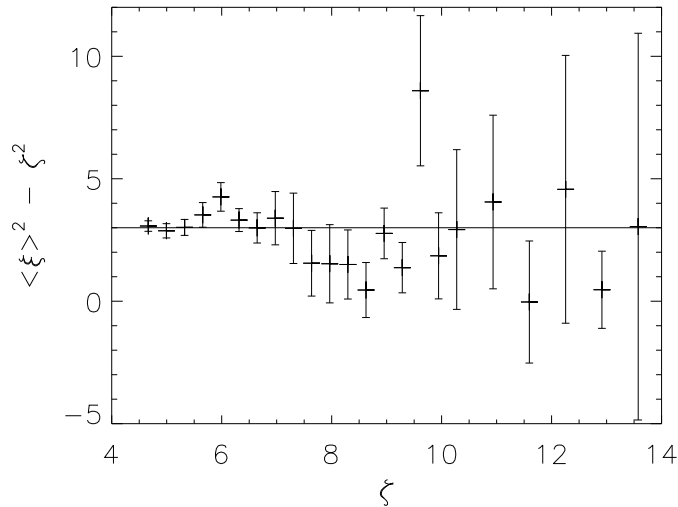


FIG. B1.— The quadratic difference between measured ζ and $\langle \xi \rangle$ (measured across 25 realizations of all noise terms), binned and plotted against a wide range of ζ . These data are consistent with $\langle \xi \rangle^2 - \zeta^2 = 3$, with $\chi^2 = 27$ for 23 degrees of freedom.

C. MASS-SIGNIFICANCE SCALING PARAMETERS

We have assumed that the scaling between ζ and M takes the form

$$\zeta = A \left(\frac{M}{5 \times 10^{14} M_{\odot} h^{-1}} \right)^B \left(\frac{1+z}{1.6} \right)^C, \quad (\text{C1})$$

where cluster mass M is defined in terms of a spherical overdensity relative to the mean density at a given redshift z and the pivot points in this relation were chosen to roughly match the mean mass and redshift of clusters in the SPT sample. Estimates for B and C were obtained from extensive simulations; in this appendix we explore various limiting cases to better understand what values are expected. For the cosmological analysis we use priors informed by our simulations.

The amplitude of the SZ effect through the center of a cluster (the central decrement) is expected to scale as (Holder & Carlstrom 1999)

$$y_0 \propto M(1+z)^3, \quad (\text{C2})$$

so if ζ is proportional to y_0 we would expect $B = 1$ and $C = 3$.

The integrated SZ flux Y ($= \int y d\Omega$) scales with mass as (Barbosa et al. 1996)

$$Y \propto M^{5/3}(1+z)/D_A(z)^2, \quad (\text{C3})$$

where Ω is the solid angle subtended by a cluster with radius R at redshift z and $D_A(z)$ is the angular diameter distance to redshift z .

For unresolved detections, where the signal to noise is simply proportional to Y divided by the noise per resolution element, we would expect $B = 5/3$. The redshift scaling is more complicated: at $z \sim 0.6$, $d_A \propto (1+z)^{1.3}$ leading to $C \sim -1.6$.

For resolved detections, the cluster is spread over several resolution elements: the number of detector resolution elements subtended by a cluster of size R scales as R^2/D_A^2 and thus the integrated noise N_{int} scales as $M^{1/3}(1+z)^{-1}D_A(z)^{-1}$ (assuming white noise). If ζ traces the integrated quantity Y/N_{int} , we obtain $\zeta \propto M^{4/3}(1+z)^2 d_A^{-1}$ and thus would expect $B \sim 4/3$ and $C \sim 0.7$ at $z \sim 0.6$.

From these scaling arguments we would expect the slope parameter B to reside within the range $1 \leq B \leq 1.66$, while C is strongly dependent on the experiment. In practice, the true scaling is likely to be influenced by a number of observational effects. For instance, small clusters are partially washed out by the $1'$ SPT beam. On the other hand, large, low-redshift clusters are de-weighted by the matched filter due to CMB confusion, reducing their detection significance (the latter could be alleviated by multi-frequency cluster detection).

To better capture the possible form of the redshift evolution in the SPT mass-significance scaling relation, a second parameter could be incorporated (for example, an additional power-law dependence on the angular diameter distance or linear evolution in the parameter C with redshift). Given the small size of the SPT sample and the uncertainties placed on the other parameters, the statistical power is insufficient to constrain such a parameter. X-ray follow up observations of the SPT cluster sample are currently underway and will shed much light on the scaling between SPT detection significance and SZ flux.

During the cosmological analysis (§5), the parameters A , B , C , and the intrinsic scatter were marginalized over with the Gaussian priors given in Table C1. The preferred scaling relation parameter values for the highest likelihood point in each of the four MCMC chains are given in Table C1. The recovered values and uncertainties on σ_8 and w are unaffected by widely varying priors on both B and C , indicating that these are not a significant source of overall uncertainty in the current analysis.

TABLE C1
PREFERRED SCALING RELATION PARAMETERS

Chain	A	B	C	$Scatter$
Λ CDM WMAP7+SPT	5.62	1.43	1.40	0.21
Λ CDM CMBall+SPT	5.46	1.43	1.38	0.21
wCDM WMAP7+SPT	6.01	1.42	1.45	0.21
wCDM WMAP7+BAO+SNe+SPT	5.42	1.44	1.41	0.21
(Gaussian Prior $\pm 1\sigma$)	6.01 ± 1.8	1.31 ± 0.26	1.6 ± 0.8	0.21 ± 0.04

NOTE. — These are the values which maximize the likelihood for the highest likelihood point in each chain. For comparison, bottom row shows the Gaussian prior assumed on each parameter during the cosmological analysis.

D. MASS ESTIMATES

To provide a mass estimate for the catalog presented here, one must estimate ζ . As mentioned in Section 4.8, ξ is a biased estimator of $\langle \xi \rangle$ and hence of ζ . In order to correct for this bias, one must make an estimate of the mass function. Although the shape of the mass function is in principle dependent on the cosmology, we find that the mass estimates are robust to exact choice of cosmology and hence assume a fiducial cosmology for the mass estimates presented in Table D1. Specifically, we use the maximum likelihood point in the Λ CDM WMAP7+SPT chain: ($\Omega_B h^2 = 0.0229$, $\Omega_C h^2 = 0.107$, $H_0 = 72.7$, $\tau = 0.0877$, $n_s(0.002) = 0.966$, $A_s(0.002) = 23.6 \times 10^{-10}$, $A = 5.62$, $B = 1.43$, $C = 1.40$, scatter = 0.21). The uncertainties in the cluster redshifts were assumed to be negligible for these purposes.

Mass estimates were obtained for an assumed mass- ξ scaling relation using Bayes' theorem and assuming that the prior probability for the mass is proportional to the Tinker et al. (2008) mass function:

$$\frac{dP(\ln M|\xi)}{d \ln M} \propto \frac{dN}{d \ln M} P(\xi|\ln M). \quad (\text{D1})$$

The probability distribution $P(\xi|\ln M)$ was found from combining the (logarithmic) intrinsic scatter in the scaling relation, as well as the (linear) scatter in ξ for each cluster. This yielded an unbiased estimate of the mass of each cluster and provided the statistical uncertainty on each mass.

The uncertainty in mass estimates caused by uncertainty in the scaling relation was calculated using a first order Taylor expansion about the best fit parameters b_k^0 , where $b_k = \{A, B, C\}$. Changes in cluster mass estimates, m_i , caused by a different assumed scaling relation are then given by $\delta m_i = \sum_k \frac{\partial m_i}{\partial b_k} (b_k - b_k^0)$. The covariance of the mass estimates is given by $\text{cov}(\delta m_i, \delta m_j) = \sum_{k,l} \frac{\partial m_i}{\partial b_k} \sigma_{kl}^2 \frac{\partial m_j}{\partial b_l}$, where σ_{kl} represents the covariance between parameters b_k and b_l . This parameter covariance was found by numerically calculating the Hessian of the 10-dimensional log-likelihood surface about the best fit parameters. In order to calculate the Hessian of the WMAP5 likelihood surface, we made use of CosmoMC package (Lewis et al. 2002). Assuming Gaussian errors, we inverted the Hessian matrix, yielding the parameter covariance. The systematic uncertainties in mass estimates reported in Table D1 are derived from the diagonal elements of $\text{cov}(\delta m_i, \delta m_j)$.

Uncertainty in the scaling relation parameters dominates the total uncertainty on the mass and the errors on the mass estimates are therefore strongly correlated. In Table D1, the statistical and systematic errors are separated. The full covariance matrix is provided at <http://pole.uchicago.edu/public/data/vanderlinde10/>.

TABLE D1
MASS ESTIMATES FOR THE SPT CLUSTER CATALOG

Object Name	ξ	z	$M_{200}(\rho_{mean})(10^{14} M_\odot h^{-1})$ mass $\pm 68\%\text{stat} \pm 68\%\text{syst}$	$M_{500}(\rho_{crit})(10^{14} M_\odot h^{-1})$ mass $\pm 68\%\text{stat} \pm 68\%\text{syst}$
SPT-CL J0509-5342	6.61	0.4626	$5.09 \pm 1.02 \pm 0.69$	$2.98 \pm 0.66 \pm 0.40$
SPT-CL J0511-5154	5.63	0.74	$3.49 \pm 0.87 \pm 0.43$	$2.15 \pm 0.57 \pm 0.26$
SPT-CL J0516-5430	9.42	0.2952	$7.84 \pm 1.29 \pm 1.25$	$4.39 \pm 0.84 \pm 0.69$
SPT-CL J0521-5104	5.45	0.72	$3.39 \pm 0.89 \pm 0.39$	$2.08 \pm 0.58 \pm 0.23$
SPT-CL J0528-5259	5.45	0.7649	$3.31 \pm 0.86 \pm 0.38$	$2.04 \pm 0.56 \pm 0.23$
SPT-CL J0533-5005	5.59	0.8811	$3.19 \pm 0.79 \pm 0.37$	$1.99 \pm 0.53 \pm 0.22$
SPT-CL J0539-5744	5.12	0.77	$3.05 \pm 0.84 \pm 0.33$	$1.89 \pm 0.55 \pm 0.20$
SPT-CL J0546-5345	7.69	1.0670	$4.02 \pm 0.72 \pm 0.55$	$2.53 \pm 0.52 \pm 0.34$
SPT-CL J0551-5709	6.13	0.4231	$4.84 \pm 1.06 \pm 0.68$	$2.81 \pm 0.67 \pm 0.39$
SPT-CL J0559-5249	9.28	0.6112	$6.16 \pm 1.02 \pm 0.85$	$3.68 \pm 0.71 \pm 0.50$
SPT-CL J2259-5617	5.29	0.1528	$4.91 \pm 1.45 \pm 0.71$	$2.68 \pm 0.82 \pm 0.38$
SPT-CL J2300-5331	5.29	0.29	$4.37 \pm 1.27 \pm 0.60$	$2.48 \pm 0.75 \pm 0.33$
SPT-CL J2301-5546	5.19	0.79	$3.07 \pm 0.84 \pm 0.30$	$1.90 \pm 0.55 \pm 0.18$
SPT-CL J2331-5051	8.04	0.5708	$5.64 \pm 0.99 \pm 0.80$	$3.36 \pm 0.67 \pm 0.46$
SPT-CL J2332-5358	7.30	0.32	$6.21 \pm 1.15 \pm 0.94$	$3.52 \pm 0.74 \pm 0.52$
SPT-CL J2337-5942	14.94	0.7815	$7.86 \pm 1.17 \pm 1.18$	$4.77 \pm 0.86 \pm 0.70$
SPT-CL J2341-5119	9.65	0.9984	$5.02 \pm 0.82 \pm 0.69$	$3.14 \pm 0.60 \pm 0.42$
SPT-CL J2342-5411	6.18	1.09	$3.21 \pm 0.70 \pm 0.43$	$2.03 \pm 0.48 \pm 0.27$
SPT-CL J2355-5056	5.89	0.35	$4.86 \pm 1.13 \pm 0.70$	$2.79 \pm 0.70 \pm 0.39$
SPT-CL J2359-5009	6.35	0.76	$3.98 \pm 0.84 \pm 0.54$	$2.45 \pm 0.57 \pm 0.32$
SPT-CL J0000-5748	5.48	0.75	$3.36 \pm 0.87 \pm 0.41$	$2.07 \pm 0.57 \pm 0.25$

NOTE. — Note that the masses $M_{500}(\rho_{crit})$ (where the overdensity is with respect to the critical density rather than the mean density) were calculated by converting from $M_{200}(\rho_{mean})$ assuming a Navarro-Frenk-White density profile and the mass-concentration relation of Duffy et al. (2008). These masses may be underestimates for low-redshift clusters ($z \lesssim 0.3$), where a power-law scaling relation fails to fully capture the behavior of the CMB-confused SZ signal, and that given for SPT-CL 2332-5358 should be considered a lower limit due to the known point source contamination.